

The Effect of Pulsar Geometry on the Observed Gamma-ray Spectrum of Millisecond Pulsars

Sheridan J. Lloyd,¹* Paula M. Chadwick¹ and Anthony M. Brown¹

¹ Centre for Advanced Instrumentation, Dept. of Physics, University of Durham, South Road, Durham, DH1 3LE, UK

Accepted 16th April 2024

ABSTRACT

We analyse 13 yrs of *Fermi*-LAT PASS 8 events from 127 gamma-ray emitting millisecond pulsars (MSPs) in the energy range 0.1–100 GeV and significantly detect 118 MSPs. We fit the stacked emission with a log parabola (LP) spectral model which we show is preferred to two previously published models. We consider the influence of pulsar properties and observer geometric effects on spectral features by defining energy flux colours for both the individual MSPs, and our stacked model as a baseline. There is no correlation of colours with pulsar luminosity, \dot{E} , surface magnetic field or magnetic impact angle. We also find that pulsar geometry has little effect on the observed gamma-ray spectrum which is in tension with previous modelling of gamma-ray emission with respect to pulsar geometry. Our LP MSP model is applicable to problems where an ensemble of gamma-ray MSPs is considered, such as that of the Galactic centre excess or in the case of emission from globular clusters.

Key words: astroparticle physics: general – gamma-rays: general – pulsars

1 INTRODUCTION

In 2009 the *Fermi*-LAT established 8 millisecond pulsars (MSPs) as pulsed gamma-ray emitters using just 8 months of observations combined with radio timing data [Abdo et al. \(2009b\)](#). The initial discoveries of [Abdo et al. \(2009b\)](#) showed that the pulse peaks of radio and gamma-ray emission in MSPs need not be co-incident, favouring different emission regions for radio and gamma-rays and supporting the prevailing slot-gap and outer gap (OG) models of gamma-ray emission ([Muslimov & Harding \(2004\)](#) and [Zhang & Cheng \(2003\)](#) respectively).

The most recent fully published catalogue of gamma-ray pulsars is "The Second *Fermi* Large Area Telescope Catalog of Gamma-Ray Pulsars" or 2PC, compiled by the *Fermi*-LAT collaboration [Abdo et al. \(2013\)](#)¹. The 2PC uses *Fermi*-LAT observations to identify 40 MSPs above 0.1 GeV.

These MSPs have short periods, $P < 6$ ms and spin-down slowly compared to young pulsars having period derivatives, \dot{P} , of 10^{-20} ss⁻¹ and spin-down power, \dot{E} , of 10^{33} – 10^{37} erg s⁻¹ as compared to 10^{33} – 10^{38} erg s⁻¹ for young pulsars. Their observed photon fluxes are $(0.2$ – $9.2) \times 10^{-8}$ cm⁻² s⁻¹ and energy fluxes $(0.3$ – $11) \times 10^{-11}$ erg cm⁻² s⁻¹. The phase-folded light curves of the

MSPs most commonly exhibit 1 or 2 pulse peaks (13 and 24 MSPs respectively), although 3 MSPs exhibit 3 pulse peaks.

The gamma-ray luminosities L_γ are 10^{32} – 10^{34} erg s⁻¹ which indicates a typical efficiency of conversion of spin-down power to gamma-ray luminosity of $\eta < 1$, with $\eta = L_\gamma/\dot{E}$. In the 2PC, η is typically 0.1 (or 10%) for MSPs but can be much higher, with one lower-luminosity MSP, J0610-2100 ($L_\gamma = 10^{33}$ erg s⁻¹) having $\eta = 10$, although this is uncommon.

At higher energies of 10 GeV–2 TeV, the 3FHL catalog of [Ajello et al. \(2017\)](#) identifies 15 MSPs at Galactic latitude $|b| \geq 10^\circ$ with 13 previously identified as pulsed gamma-ray emitters at lower energies using the LAT and the remaining 2 radio pulsars previously undetected in gamma-rays.

In a more recent study than the 2PC, an analysis of 19 MSPs with 7 years of PASS 8 *Fermi*-LAT event data in the range 0.1–300 GeV shows that the empirical MSP death-line (or \dot{E} below which gamma-ray emission cannot be detected) is 8×10^{32} erg s⁻¹ [Guillemot et al. \(2016\)](#). This analysis also demonstrates that L_γ is uncorrelated with \dot{E} , showing a nearly 2 orders of magnitude of scatter for MSPs with an \dot{E} of 10^{34} erg s⁻¹. For $\dot{E} > 5 \times 10^{34}$ erg s⁻¹, L_γ is directly proportional to $\sqrt{\dot{E}}$. Similarly the wide variation of the relationship between η , L_γ and \dot{E} makes it difficult to deduce gamma-ray luminosities *a priori* from MSP timing information alone.

In contrast, the geometry of individual MSPs is increasingly well understood, through the fitting of models to gamma-ray and radio light curves, with the angles for both the line of sight and magnetic axis, with respect to the pulsar spin axis determined, for

* E-mail: sheridan.j.lloyd@durham.ac.uk (SJL)

¹ A successor catalogue to the 2PC, the 3PC was published recently and does not impact this work [Smith et al. \(2023\)](#).

all 40 MSPs in the 2PC Johnson et al. (2014) and more recently for 10 MSPs with high signal-to-noise observations Benli et al. (2021).

We note that there is recent modelling and interest in the effects of pulsar inclination (among other variables) on the observed gamma-ray spectra of MSPs ranging from a general one Viganò et al. (2015a,b), to a spectral softening below 400 MeV, to being a lesser influence on the high-energy spectrum Torres et al. (2019); Giraud & Petri (2021). Thus, the effect of pulsar magnetosphere geometry and magnetic inclination angle on the observed gamma-ray spectra is an open question. Therefore, inclination effects could well affect the the observed gamma-ray spectrum, although to our knowledge this has not been confirmed by observation.

A demonstrable link between pulsar inclination and observed spectra could serve as a constraint on spectral emission models where the pulsar geometry is known, whilst conversely the geometry of the pulsar system may be constrained from the observed gamma-ray spectrum. We are therefore motivated in this paper to determine for the first time if there is a link between pulsar geometry and observed gamma-ray spectral features.

In this work, we seek to construct the best general spectral model for 118 MSPs and use it to examine the effect of geometry on gamma-ray spectra, whilst excluding any systematic effect of other pulsar properties (surface magnetic field, luminosity, \dot{E}). We analyse a larger sample of 127 MSPs, rather than the 39 MSPs of the 2PC Abdo et al. (2013), as used by the previous stacked MSP analyses of Xing & Wang (2016) and McCann (2015). Furthermore, we note that the MSP spectral model we produce is very useful in its own right, and could be applied to any problem where gamma-ray emission is presumed to originate from an ensemble of MSPs plus another component such as emission from dark matter, as relevant to globular clusters or the Galactic centre excess.

This paper is structured as follows. In Section 2 we describe the selection criteria of MSPs for analysis. In Section 3 we describe our analysis method for the detection of MSPs, and in Section 4 we present our results. In Section 5 we derive a spectral model for the stacked emission of detected MSPs. In Appendix A we compare our model to those of Xing & Wang (2016) and McCann (2015) and determine whether there is any relationship between colours constructed from low and medium energy MSP fluxes, and pulsar \dot{E} , luminosity and surface magnetic field. We also consider the spectral predictions of synchro-curvature emission models incorporating pulsar magnetic inclination and determine if they are suitable for comparison with the observed gamma-ray spectra. Finally in Section 7 we summarise our findings and make suggestions for future work.

2 MILLISECOND PULSAR SELECTION

We select all 127 MSPs (defined as any pulsar with period ≤ 30 ms) from the Public List of LAT Detected Gamma-Ray Pulsars². Their co-ordinates, periods and \dot{E} values are shown in Table D1.

² <https://confluence.slac.stanford.edu/display/GLAMCOG/Public+List+of+LAT+Detected+Gamma-Ray+Pulsars>, accessed on 24th August 2021

3 ANALYSIS METHOD

3.1 Initial Photon Event Data Selection

The data in this analysis were collected by *Fermi*-LAT between 4th Aug 2008 (15:43 h) to 26th August 2021 (00:52 h), (Mission Elapsed Time (MET) 2395574147[s] to 651631981[s]). We select all PASS 8 events which are *source* class photons (evclass = 128), and PSF3 events with the best quartile direction reconstruction, (evtype = 32), spanning the energy range 0.1–100 GeV. Throughout our analysis, the *Fermipy* software package³ with version 2.0.8 of the *Fermitools* is used, in conjunction with the P8R3_SOURCE_V3 instrument response functions. We apply the standard PASS8 cuts to the data, including a zenith angle 90° cut to exclude photons from the Earth limb, and good-time-interval cuts of DATA_QUAL > 0 and LAT_CONFIG = 1. The energy binning used is 4 bins per decade in energy and spatial binning is 0.1° per image pixel.

3.1.1 Spectral Models

The differential flux, dN/dE , (photon flux per energy bin) of an individual MSP, is described by a spectral model which is either an exponential cut-off power law 2 (Eqn. 1, PLSuperExpCutoff2), a log parabola (Eqn. 2, LP), or a power law (Eqn. 3, PL)⁴.

$$\frac{dN}{dE} = N_0 \left(\frac{E}{E_0} \right)^{\gamma_1} \exp \left((-aE)^{\gamma_2} \right) \quad (1)$$

where *normalisation* (also known as *prefactor*) = N_0 , *index1* = γ_1 , E_0 is the scale, a is the exponential factor and *index2* = γ_2 (which controls the sharpness of the exponential cut-off).

$$\frac{dN}{dE} = N_0 \left(\frac{E}{E_b} \right)^{-(\alpha + \beta \log(E/E_b))} \quad (2)$$

where *norm* = N_0 , and E_b is a *scale* parameter.

$$\frac{dN}{dE} = N_0 \left(\frac{E}{E_0} \right)^{\gamma} \quad (3)$$

where *prefactor* = N_0 , *index* = γ and *scale* = E_0 .

3.2 MSP Likelihood Analysis

We perform a full likelihood analysis on all 127 MSP targets (Table D1), in the energy range 0.1–100 GeV, using a 25° Radius of Interest (ROI) centred on the nominal MSP co-ordinates and a 40° Source Radius of Interest (SROI) for each MSP target. The model we use in our likelihood analysis consists of a point source population seeded from the *Fermi*-LAT's 10 yr fourth point source catalog, data release 2, (4FGL-DR2, gll_psc_v27.fit), extended gamma-ray sources and diffuse gamma-ray emission. The diffuse emission detected by the *Fermi*-LAT consists of two components: the Galactic diffuse flux, and the isotropic diffuse flux. The Galactic component is modelled with *Fermi*-LAT's gll_iem_v07.fit spatial map with the normalisation free to vary. The isotropic diffuse emission is defined by *Fermi*'s iso_P8R3_SOURCE_V3_PSF3_v1.txt tabulated spectral data. The normalisation of the isotropic emission is left free to vary.

³ *Fermipy* change log version 1.0.1 (Wood et al. (2017))

⁴ As described in the FSSC source model FSSC (2010)

In addition, all known sources (including MSPs) take initial spectral parameters and position from the 4FGL.

Initially, the *setup* and *optimize* methods are run to create count and photon exposure maps and to compute the test statistic (TS) values of all 4FGL sources in the model. The TS value is defined as Eqn. 4 where L_0 is the maximum likelihood for a model without a source observations (i.e. the null hypothesis) and L_1 is the maximum likelihood for an additional source observation at a given location.

$$TS \equiv -2(\ln L_0 - \ln L_1) \quad (4)$$

The *fit* method is then run: *fit* is a likelihood optimisation method which executes a fit of all parameters that are currently free in the the model and updates the TS and predicted count (N_{pred}) values of all sources. From this fit, all point sources with a $TS < 4$, or with a predicted number of photons < 4 are removed from the model.

The normalisation of all sources within 10° of the MSP are then freed using the *free_source* method to allow for the Point Spread Function (PSF) of PSF3 events down to 100 MeV (95 % containment at 8°). The source nearest to the catalogue position of the MSP has *prefactor* and *index* spectral parameters (Eqn. 3) freed for power law sources and *prefactor*, *index1* and *exfactor* freed for PLSuperExpCutoff2 sources (Eqn. 1).

The shape and normalisation parameters of all sources with a $TS > 25$ are then individually fitted using the *optimize* method. Then the *fit* method is run twice more with an intervening *find_sources* step. *Find_sources* is a peak detection algorithm which analyses the test statistic (TS) map to find new sources over and above those defined in the 4FGL model by placing a test point source, defined as a power law (PL) with spectral index 2.0, at each pixel on the TS map and recomputing likelihood. Finally, the *sed* method generates a spectral energy distribution, with energy dispersion disabled for all MSPs which are known 4FGL sources, and a 2σ confidence limit on the determination of instrument upper limits.

4 ANALYSIS RESULTS

We detect 118 of the 127 catalogue MSPs in the energy range 0.1–100 GeV at a significance of 5σ (test statistic, $TS=25$) or greater. The 9 MSPs, J0154+1833, J0636+5129, J1327-0755, J1946+3417, J1455-3330, J1909-3744, J1832-0836, J2205+6012 and J2317+1439 are undetected through their integrated emission in our study, but 6 of these are detectable in other work by phase folded pulsed emission using a radio ephemeris Smith et al. (2019, 2017). We list the TS, offset from catalogue co-ordinates, and energy and photon fluxes in Table B1.

We also list the best fit spectral models for MSPs with a PLSuperExpCutoff2, LP or PL spectral model, in Tables C1, C2 and C3, respectively. For these spectral models we provide a selection of representative spectral energy distributions in Figs. C1 and C2.

We determine the average differential energy flux per energy bin (for flux points of $\geq 2\sigma$ significance) and the standard error of the mean for the detected MSPs (Table 1). The energy bin centres and lower and upper bin energy (extent) arise from a binning of 4 bins per decade of energy as specified in the analysis. Note that the error (energy dispersion) of the bin extent is $< 10\%$ between 1–100 GeV increasing to 20 % at 0.1 GeV.

The majority of MSPs display emission across the whole energy range between 0.2–10 GeV, while emission between 10–18

GeV is seen in only 41 % of MSPs, and 15 % of MSPs above 18 GeV.

5 GEOMETRIC EFFECTS ON THE OBSERVED GAMMA-RAY SPECTRA OF MILLISECOND PULSARS

The geometry of a pulsar system is described by (1) the angle between the observer line-of-sight (LOS) and the pulsar spin axis (ζ), (2) the angle between magnetic axis and the pulsar spin axis, also known as the magnetic obliquity (α) and (3) the orbital inclination angle between the pulsar orbital plane and the observer LOS (i). An impact parameter (β) describing the closest approach of the magnetic axis and the LOS is defined as $\beta = \zeta - \alpha$ as in Johnson et al. (2014).

In Guillemot & Tauris (2014), i is derived for Galactic field MSPs, with helium white dwarfs as binary companions, from the relationship of pulsar and white dwarf mass, and the orbital period. Over the life of the system, the values of i and ζ with respect to the pulsar rotation axis are shown to align, with the detection of gamma-ray emission in Galactic MSPs appearing to be somewhat favoured by smaller values of ζ .

In Vigano et al. (2015a) the effect of parameters and assumptions in the OG model are examined. The magnetic inclination angle of a pulsar is shown to affect the magnetosphere geometry, position of the OG and radius of curvature (r_c). r_c is identified as the most important parameter having an order of magnitude impact on the parallel electric field, (responsible for lepton acceleration and consequent curvature radiation), which is noted to affect the observed gamma-ray spectrum qualitatively.

In their follow-up paper, Vigano et al. (2015b) model exemplar pulsar gamma-ray spectra obtained by integrating the energy loss of a single particle with distance travelled, convolved with an effective observed particle distribution which incorporates geometry and beaming effects. They show that photons from the initial part of the particle trajectory exhibit softer low energy spectra below 200 MeV, with an index of 0.68 vs an index of 1.14 for emission from the whole trajectory. They note that such spectra could be observed for pulsars with a favourable viewing geometry of the outer gap.

The effect of inclination on the observed gamma-ray spectrum is also considered by Cerutti et al. (2016) who model the combined low-energy synchro-curvature radiation from the polar cap and higher-energy pulsar synchrotron radiation (HES) from the equatorial current sheet (ECS) using a particle-in-cell (PIC) simulation. They produce phase-averaged observed pulsar energy spectra between 400 keV – 4 GeV for varying α and ζ . These spectra show a trend of decreasing energy flux and a softening of the spectrum between 40–400 MeV, with the disappearance of the HES spectral peak at ~ 200 MeV as β decreases from 90° to 0° for $\zeta = 90^\circ$. In contrast, varying α from 0 to 90° for ζ angles of 45° and 60° generally results in few spectral shape changes.

In Petri (2019), a minimalist model determines lepton particle trajectories and velocities depending only on local B field using the vacuum rotator dipole model (VRDM) of pulsars as first described by Deutsch (1955). The gamma-ray spectrum arising from the resulting curvature radiation is determined and used to produce sky-maps and light curves for varying pulsar phase, angle ζ and magnetic inclination angle (χ in that paper rather than α), with respect to the pulsar rotation axis. This modelling is able to reproduce spectral cut-offs at a few GeV and single or double peaked light curves broadly consistent with Fermi-LAT observations of pulsars. It is also shown that there is a slight hardening of the spectrum be-

Bin Centre GeV	Lower Bin Energy GeV	Upper Bin Energy GeV	MSP Count and Percentage of Sample with Significant Flux in Bin	Mean Energy Flux $10^{-6} \text{ MeV cm}^{-2} \text{ s}^{-1}$
0.13	0.10	0.18	28 (23.7)	2.23 ± 0.34
0.24	0.18	0.32	85 (72.0)	2.30 ± 0.20
0.42	0.32	0.56	106 (89.8)	2.49 ± 0.24
0.75	0.56	1.00	112 (94.9)	2.77 ± 0.29
1.33	1.00	1.78	114 (96.6)	2.97 ± 0.32
2.37	1.78	3.16	116 (98.3)	2.71 ± 0.30
4.22	3.16	5.62	112 (94.9)	2.21 ± 0.28
7.50	5.62	10.00	92 (78.0)	1.37 ± 0.22
13.34	10.00	17.78	48 (40.7)	0.87 ± 0.17
23.71	17.78	31.62	18 (15.3)	0.73 ± 0.17
42.17	31.62	56.23	7 (5.9)	0.56 ± 0.11
74.99	56.23	100.00	1 (0.8)	0.09 ± 0.00

Table 1. The count and percentage of significant ($> 2\sigma$) flux points for detected MSPs along with mean flux and associated standard error of the mean.

tween 1–10 GeV, when the annulus of the emitting region increases in extent, as it moves closer to the surface of the star, from $0.5-1$ of the light cylinder radius (R_{LC}) to $0.1-1 R_{LC}$. Beyond the light cylinder there is no change in emission spectrum with increasing extent ($1-5 R_{LC}$). Overall the spectral shape is noted to be insensitive to geometry.

In [Torres et al. \(2019\)](#), a synchrocurvature spectral emission model is able to reproduce well the observed spectral energy distribution of 18 out of 32 non-MSPs⁵ considered, from X-ray to gamma-ray energies. The free parameters of the model are properties intrinsic to the pulsar, namely, the parallel electric field and the magnetic field gradient, and properties related to the viewing geometry of the observer: a length scale for particle emission relative to the radius of the light cylinder and a normalisation of the accelerated particle distribution with respect to distance ($x_0/R_{LC}, N_0$ respectively). This model can reproduce the gamma-ray spectrum of the 4 MSPs considered but not the X-ray spectrum, whilst 3 other MSPs can be well fitted simultaneously in X-rays and gamma-rays. Extending the model so that there are two emission regions (each with own values of $(x_0/R_{LC}, N_0)$, but same intrinsic properties) and visible to a varying extent depending on observer line-of-sight, is shown to fit both the X-ray and gamma-ray observations. This suggests that, whilst broad-band emission from X-rays to gamma-rays can be sensitive to geometric effects and the visibility of different emission regions, gamma-ray emission is less so. The authors also note that the precise location and extent of the accelerating region has previously been shown not to dominate the predicted high-energy spectral shape.

Finally, [Giraud & Petri \(2021\)](#) model the gamma-ray emission arising from synchrotron and curvature radiation in high-altitude slot gaps at the separatrix between open and closed field lines in the pulsar magnetosphere for pulsars of period 2 ms. They use a VRDM with a mono-energetic lepton distribution to produce phase-integrated and LOS averaged photon count spectra between 1–30 GeV, with spectral shape and energy limits that vary with magnetic obliquity, χ , and LOS, ζ , whilst retaining a spectral peak at around 4 GeV. Specifically, increasing the magnetic obliquity (for phase and line of sight averaged spectra) from 30 to 90° increases spectral energy limits from 7 to 30 GeV. However, they conclude that, while

the pulsar radio spectra significantly depend on the magnetic obliquity, the high-energy part of the spectrum is much less sensitive to geometry.

The models of [Cerutti et al. \(2016\)](#); [Petri \(2019\)](#); [Torres et al. \(2019\)](#); [Giraud & Petri \(2021\)](#) are broadly similar in that they (1) derive the curvature radiation spectrum using a Bessel function of order $5/3$, (2) are force-free allowing leptons to travel along magnetic field lines, because the screening of the pulsar electric field by plasma is excluded and (3) balance lepton acceleration and braking due to radiative friction. [Petri \(2019\)](#) and [Giraud & Petri \(2021\)](#) employ a mono-energetic particle distribution whereas [Torres et al. \(2019\)](#) spatially vary the number density of particles.

For the models above, we summarise the effect of geometry on the gamma-ray spectrum in Table 2, varying from no effect to changes in energy limits and spectral shape with varying α . However, the models which present explicit spectra for specific geometries are difficult to compare directly with gamma-ray observations of MSPs, as they either do not provide a full co-varying range of ζ and α ([Giraud & Petri \(2021\)](#)), or are designed to test a model concept rather than to be fitted directly to observations ([Cerutti et al. \(2016\)](#)), and moreover they do not reproduce gamma-ray spectral peaks of a few GeV as seen in MSPs.

As no model spectra are suitable for comparison with observations, we instead consider the observed MSP gamma-ray spectrum to investigate if geometry has any systematic effect.

Specifically, we would like to examine the most rapidly varying part of the MSP spectrum, which is generally away from the cut-off values of the the exponential power law in the 2PC (1.2–5.3 GeV), where the spectrum peaks and is often almost flat. Moreover, we wish to probe energy ranges which are noted as being sensitive to emission extent and geometric effects as in Table 2 above.

We therefore define two colour band ratios to examine the requisite energy ranges, a low-energy ratio, (Eqn. 5, LE) and a medium energy ratio, (Eqn. 6, ME).

$$LE = \frac{\text{Energy Flux}_{133 \text{ MeV}}}{\text{Energy Flux}_{237 \text{ MeV}}} \quad (5)$$

$$ME = \frac{\text{Energy Flux}_{4217 \text{ MeV}}}{\text{Energy Flux}_{7499 \text{ MeV}}} \quad (6)$$

The precise energy centres and limits for LE and ME arise from the binning employed, but the energy bins are also chosen to examine the varying and potentially inclination-sensitive part of the

⁵ Although their selection criteria for a non-MSP is a pulsar with period > 10 ms, their 18 pulsars all have period > 30 ms and thus also meet our definition of a non-MSP.

Model Reference	Inclination Effect on MSP gamma-ray Spectrum
Petri (2019)	Overall, the spectral shape is insensitive to geometry.
Torres et al. (2019)	Gamma-ray spectrum insensitive to geometry but two visible emission regions needed to account for both X-ray and gamma-ray emission.
Vigano et al. (2015a)	Qualitatively, magnetic inclination affects spectrum via influence on radius of curvature and the consequent parallel electric field.
Vigano et al. (2015b)	Favourable viewing geometry sampling initial particle trajectories produces softer low-energy spectra.
Cerutti et al. (2016)	A proof of concept model showing spectral softening below 400 MeV for $\zeta=90^\circ$ as α increases, in contrast with few spectral shape changes for $\zeta = 45$ and 60° .
Giraud & Petri (2021)	Increasing magnetic inclination increases upper energy limit of ζ averaged photon spectra from 7 to 30 GeV but high-energy spectra noted to be much less sensitive to geometry than radio bands.

Table 2. Summary of inclination effects on gamma-ray spectra as indicated by current models, varying from no effect, to changes in model spectra as magnetic obliquity, α , varies

MSP spectrum as noted above. If an upper limit (UL) is present at 133 MeV or 7498 MeV, then the LE and ME colours represent upper and lower limits respectively.

If a decreasing value of β results in an increasingly soft spectrum below 400 MeV as in Cerutti et al. (2016) then we should expect a corresponding increase in the LE colour as β decreases from 90 to -45° . Conversely, if geometric effects systematically affect the spectrum between 1–10 GeV then this should appear as a changing ME colour as β changes, with the caveat that increasing emission extent from within the light cylinder could result in a decreasing ME colour.

6 THE STACKED MSP SPECTRUM

Whilst we consider the effect of geometry on the spectra of individual MSPs, these spectra can vary between MSPs, and so we must derive a stacked MSP model to serve as a baseline to show if there are systematic spectral changes depending on geometry across the MSP sample. In order to derive this model for an ensemble of Galactic field MSPs, we sum the energy fluxes ($E^2 \frac{dN}{dE}$) in each bin (ignoring ULs) between 0.1–56.2 GeV for MSPs detected in the energy range 0.1–100 GeV, with the upper energy range of 56.2 GeV arising solely from the binning employed. We exclude the 1 flux point above 56.2 GeV (for the single MSP detection J1903-7051) from the stacked model, as this flux is only marginally significant (TS 5.5).

We define two models for comparison; a super exponential

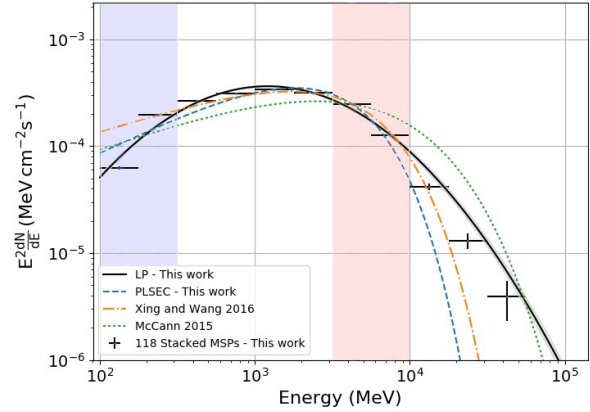


Figure 1. The likelihood best-fit models for LP and PLSEC (both this work), McCann, and Xing and Wang for the stacked spectrum of 118 MSPs. The LP model is the best fit overall and has just visible 1σ uncertainty indicated by grey shading. The blue and red bands (each comprising two bins), indicate the overall energy range used to form the low and medium energy colours respectively as in Eqns. 5 and 6. For clarity the uncertainty of the McCann (1σ) and the Xing and Wang (3σ) models is not shown.

Parameter	Value	Unit
α	1.88 ± 0.01	-
β	$(3.16 \pm 0.04) \times 10^{-1}$	-
Normalisation	$(3.49 \pm 0.02) \times 10^{-4}$	$\text{cm}^{-2} \text{s}^{-1} \text{TeV}^{-1}$
Scale	1×10^{-3}	TeV

Table 3. The parameters of the best-fit LP model (this work) using Eqn. 2, for the stacked differential energy flux of 118 significantly detected MSPs in the energy range 100 MeV–56.2 GeV. The LP model is the best fit overall compared to all other models considered.

cut-off power law model spectral model as Eqn. 1, "PLSEC" and a log parabola model as Eqn. 2, "LP".

In the PLSEC model, the parameters *index1*, *Normalisation* and *exponential factor* are left free. The *scale* and *index2* parameters are frozen to 1×10^{-3} TeV and 1 respectively. In the LP model, the *Norm*, α and β parameters are left free, while E_b is frozen at 1 TeV.

We then use `GAMMAPY` version 0.18.2⁶ software to fit the flux summation of 118 MSPs with the LP and PLSEC models in the range 100 MeV–56.2 GeV.

In Appendix A we show that the LP model is the best model to describe the stacked spectrum of the 118 MSPs and preferred to the previously published models of Xing & Wang (2016) and McCann (2015). The parameters of our best fit LP model are presented in Table 3 and all models are presented alongside the stacked MSP spectrum in In Fig. 1.

The LE and ME colours for this LP model are 0.50 ± 0.02 and 1.75 ± 0.05 respectively. These serve as a baseline model to determine spectral trends for individual MSPs in our selection. We show the energy range used to form the LE and ME colour ratios on Fig. 1.

⁶ Available from <https://docs.gammapy.org/0.18.2/>

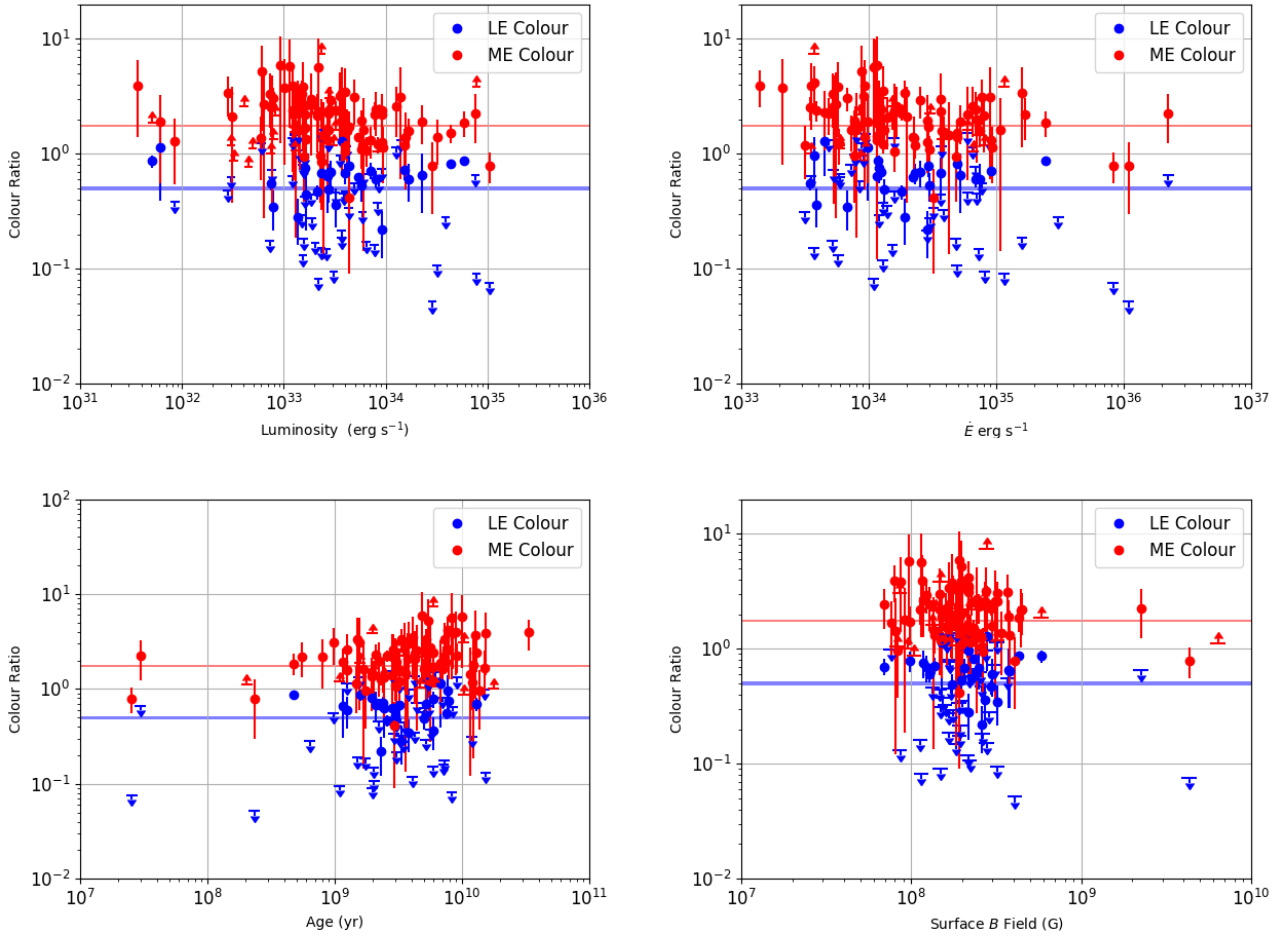


Figure 2. The LE and ME colours for the 118 MSPs plotted against pulsar luminosity, \dot{E} , characteristic age and surface magnetic (B) field. There is no apparent correlation with LE and ME colours distributed evenly above and below the LP colour values (red and blue bands). Colour ratios are shown either as points with errors (where flux points exist in all bins for the colour), or as upper or lower limits where there are a mixture of upper limit and flux point observations in the energy bands used to form the colour ratios.

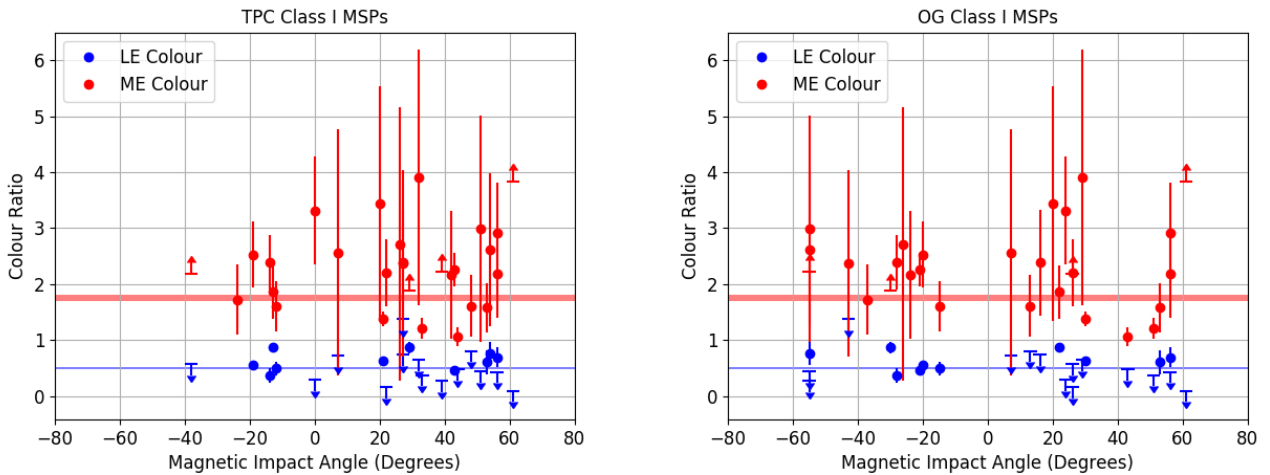


Figure 3. The LE and ME colours for Class I MSPs vs a magnetic impact angle (β) from inclination angles in Johnson et al. (2014) for a two-pole caustic model (TPC), and an outer-gap (OG) model. There is no apparent correlation of colour and impact angle. The LP colour values are shown as red and blue bands. Colour ratios are shown either as points with errors, or as upper or lower limits.

In considering the effect of inclination on spectra, we firstly need to exclude any correlation of LE and ME colours with intrinsic pulsar properties such as \dot{E} , luminosity or characteristic age ($P/2\dot{P}$). A plot of MSP spectral colours against luminosity, \dot{E} , age and surface magnetic field indicates that there is no detectable correlation (Fig. 2, Pearson correlation coefficient for ME colours of -0.23, -0.13, -0.30 and -0.16 respectively)

We next consider whether the inclination (geometric) properties of the MSP, such as the LOS, ζ , and the magnetic inclination angle, α , with respect to the pulsar rotation axis might affect spectral features. Johnson et al. (2014) use a VRDM to derive the best fit ζ and α values, for the MSPs of the 2PC. They divide the MSPs into 3 classes, Class I, II and III, defined as the MSP's gamma-ray pulse trailing, aligned or leading the MSP's radio pulse, respectively. They then derive inclination angles from a two-pole caustic (TPC) and outer-gap (OG) model for Class I MSPs, a TPC, OG and slot-gap model for Class II MSPs and a pair-starved polar cap model for Class III. We use these magnetic inclination angles to determine the magnetic impact angle, β , defined as $\beta = \zeta - \alpha$ for the three classes of MSPs (Tables 4, 5 and 6). We then plot β for individual MSP colours in Fig. 3, 4, 5. We observe that there is no dependence of ME and LE colours on β , implying that LE and ME gamma-ray spectral features of MSPs are not correlated with magnetic inclination and line-of-sight effects.

More recently, Benli et al. (2021) determine ζ and α for 10 of the same Class I MSPs as Johnson et al. (2014), using a force-free magnetospheric model for gamma-ray emission at the light cylinder and into the striped wind, and radio emission from the polar-cap to reproduce gamma-ray and radio light curves from the 2PC. They then fit the time-lag between radio and first gamma-ray pulse along with the gamma-ray pulse separation and ratio of the gamma-ray pulse heights of light curves in the 2PC for varying inclination and magnetic angle to obtain a best fit. We again determine β from their inclination and magnetic angles (Table 7).

We then plot ζ , α and β for MSPs in our selection in Fig. 6. The values of ζ and α are uncorrelated with the model colours we have calculated. However, for β , there is some indication of harder ME emission for absolute β values of 5–10° (ME colour ratio ~1) and generally softer emission outside this range, (ME colour ratio > 2), suggesting that ME spectral features are influenced by the offset of the emission region from the pulsar spin axis, once geometric viewing effects are allowed for. However, the inclination angles of more MSPs would need to be determined with the same force-free model to draw a definitive conclusion, especially as no such effect is seen when using the inclination angles of Johnson et al. (2014).

In conclusion, it appears that pulsar line-of-sight and the magnetic axis inclination seem to have little effect on the observed gamma-ray spectrum at low and medium energies. Therefore the observed gamma-ray spectrum does not allow us to constrain pulsar geometry or to further validate the existing synchro-curvature models of pulsar emission which incorporate geometric effects. However, ζ and α are determined only for a relatively small pulsar population and so we cannot completely exclude spectral differences arising from pulsar geometry.

Our standalone LP model is also useful in its own right to model ensemble emission from a population of MSPs. Such an application of a stacked MSP model is demonstrated in Brown et al. (2018), wherein, the gamma-ray emission of the globular cluster 47 Tuc is modeled using the MSP model of Xing & Wang (2016) combined with an annihilating dark matter (DM) model to show that a "MSP+DM" model is preferred over MSP emission alone. In this regard we expect our LP model comprising a larger sample

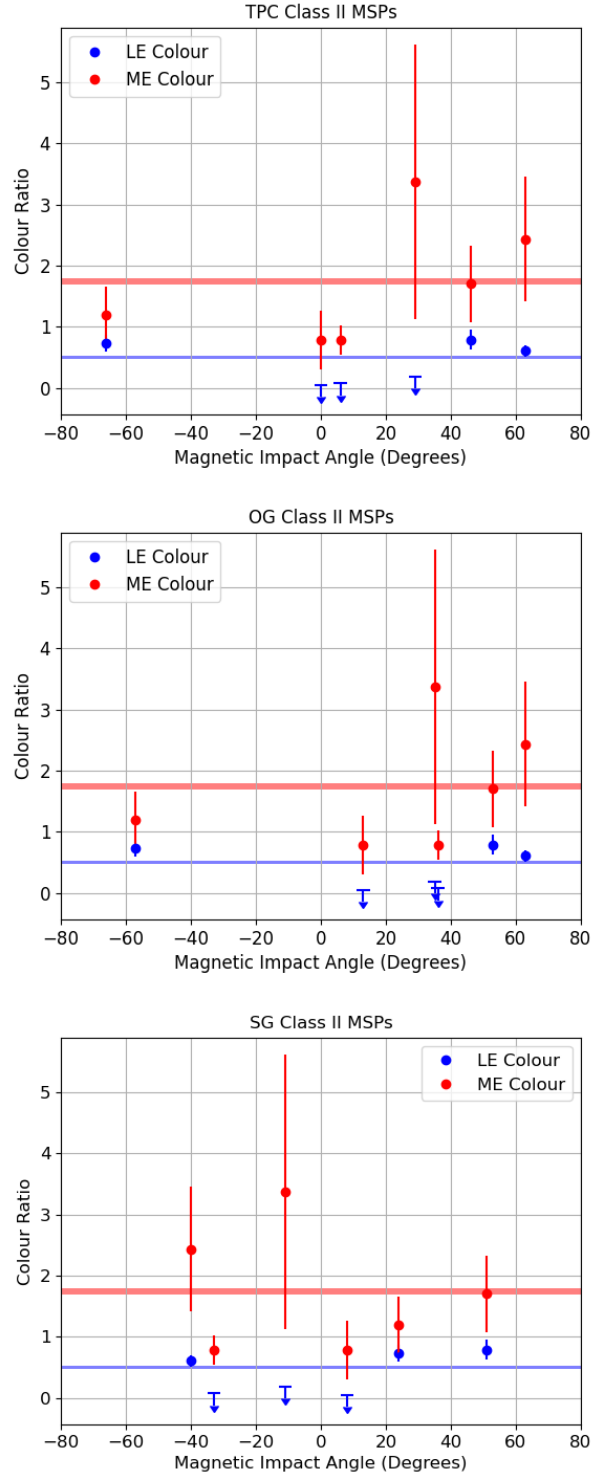


Figure 4. The LE and ME colours for Class II MSPs vs a magnetic impact angle (β) determined from inclination angles in Johnson et al. (2014) for a two-pole caustic (TPC), an outer-gap (OG) and a slot-gap (SG) model. There is no apparent correlation of colour and impact angle. The LP colour values are shown as red and blue bands. Colour ratios are shown either as points with errors, or as upper or lower limits.

MSP	TPC			OG		
	α ($^\circ$)	ζ ($^\circ$)	β ($^\circ$)	α ($^\circ$)	ζ ($^\circ$)	β ($^\circ$)
J0023+0923	38	65	27	67	24	-43
J0030+0451	74	55	-19	88	68	-20
J0101-6422	30	84	54	90	35	-55
J0102+4839	43	70	27	60	76	16
J0218+4232	25	12	-13	45	67	22
J0437-4715	35	64	29	76	46	-30
J0610-2100	87	49	-38	63	89	26
J0613-0200	55	43	-12	60	45	-15
J0614-3329	63	84	21	58	88	30
J0751+1807	21	69	48	59	72	13
J1024-0719	66	73	7	66	73	7
J1124-3653	13	69	56	17	73	56
J1125-5825	29	71	42	84	60	-24
J1231-1411	26	69	43	88	67	-21
J1446-4701	17	68	51	80	25	-55
J1514-4946	24	68	44	25	68	43
J1600-3053	61	37	-24	65	28	-37
J1614-2230	80	80	0	64	88	24
J1658-5324	30	69	39	78	23	-55
J1713+0747	36	68	32	36	65	29
J1747-4036	19	80	61	19	80	61
J2017+0603	34	67	33	23	74	51
J2043+1711	54	76	22	53	79	26
J2047+1053	51	71	20	51	71	20
J2051-0827	43	69	26	68	42	-26
J2215+5135	18	71	53	18	71	53
J2241-5236	20	76	56	19	75	56
J2302+4442	60	46	-14	65	37	-28

Table 4. Magnetic impact angle (β) for Class I MSPs determined from inclination angles in [Johnson et al. \(2014\)](#) provided for a two-pole caustic model (TPC), and an outer-gap (OG) model.

MSP	TPC			OG			SG		
	α ($^\circ$)	ζ ($^\circ$)	β ($^\circ$)	α ($^\circ$)	ζ ($^\circ$)	β ($^\circ$)	α ($^\circ$)	ζ ($^\circ$)	β ($^\circ$)
J0034-0534	23	69	46	22	75	53	23	74	51
J1810+1744	82	16	-66	81	24	-57	5	29	24
J1823-3021A	46	52	6	42	78	36	78	45	-33
J1902-5105	10	73	63	10	73	63	56	16	-40
J1939+2134	88	88	0	72	85	13	33	41	8
J1959+2048	56	85	29	52	87	35	46	35	-11

Table 5. Magnetic impact angle (β) for Class II MSPs determined from inclination angles in [Johnson et al. \(2014\)](#) provided for a two-pole caustic (TPC), an outer-gap (OG) and a slot-gap (SG) model.

MSP	α ($^\circ$)	ζ ($^\circ$)	β ($^\circ$)
J0340+4130	43	73	30
J1741+1351	46	80	34
J1744-1134	51	85	34
J1858-2216	42	74	32
J2124-3358	19	25	6
J2214+3000	59	86	27

Table 6. Magnetic impact angle (β) for Class III MSPs determined for inclination angles in [Johnson et al. \(2014\)](#) provided for a pair-starved polar cap (PSPC) model.

MSP	α ($^\circ$)	ζ ($^\circ$)	β ($^\circ$)
J0030+0451	70	60	-10
J0102+4839	55	70	15
J0437-4715	45	40	-5
J0614-3329	75	56	-19
J1124-3653	65	46	-19
J1514-4946	55	62	7
J1614-2230	85	86	1
J2017+0603	55	48	-7
J2043+1711	55	74	19
J2302+4442	50	60	10

Table 7. Magnetic impact angle (β) for Class I MSPs determined from inclination angles provided in [Benli et al. \(2021\)](#).

of 118 MSPs with well constrained 1σ errors (Fig. 1) to be more representative of an MSP ensemble than that of [Xing & Wang \(2016\)](#) which uses just 39 MSPs, a much greater 3σ uncertainty and only

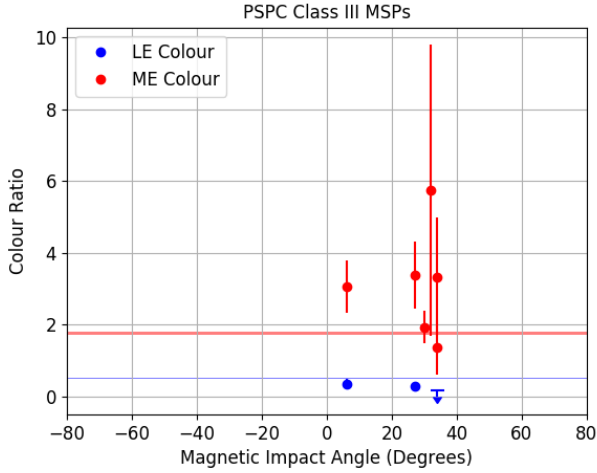


Figure 5. The LE and ME colours for Class III MSPs vs a magnetic impact angle (β) determined from inclination angles in Johnson et al. (2014), for a pair-starved polar cap (PSPC) model. There is no apparent correlation of colour and impact angle. The LP colour values are shown as red and blue bands.

57 % of the photon exposure of our study. The caveat applies that any stacked spectrum should be applied to systems only where the total spectral variation of individual MSPs is less than the model hypothesis under consideration, as demonstrated by the comment on Brown et al. (2018) in Bartels & Edwards (2019) and its reply in Brown et al. (2019). Specifically, our model will be applicable to considering the ensemble gamma-ray emission from MSPs in globular clusters (GCs, Abdo et al. (2009a)), as the characteristic ages⁷ of 76 GC MSPs ($2.6 \times 10^7 - 6.8 \times 10^{10}$ yrs) are consistent with those of the model MSPs in Fig. 2. Furthermore, the spectra of disc and bulge MSPs are consistent within uncertainties (Ploeg et al. (2020)) and so we expect our model based on local disc MSPs to be useful in consideration of the Galactic centre excess problem which could arise from an unresolved population of MSPs (Abazajian (2011)).

7 CONCLUSION

We analyse 127 MSPs from the Public List of LAT Detected Gamma-Ray Pulsars and detect 118 MSPs in the range 100 MeV–100 GeV. We sum the 100 MeV–56.2 GeV fluxes of these MSPs and find the best fit to the resulting spectral energy distribution is an LP model and that this model is superior to other published models of stacked MSP emission.

Most previous models of gamma-ray emission from MSPs suggest that pulsar geometry may affect the observed gamma-ray spectrum. These models are difficult to compare with observations as they are either qualitative, do not cover the full range of geometries or are a proof-of-concept of modelling technique which does not reproduce known features of MSP spectra.

In the absence of quantitative spectral emission models for comparison, we use our LP model as a baseline to determine if

⁷ Calculated for the list of MSPs in GCs (with period and positive period derivative) maintained at <http://www.naic.edu/~pfreire/GCpsr.html> accessed 29/10/2022

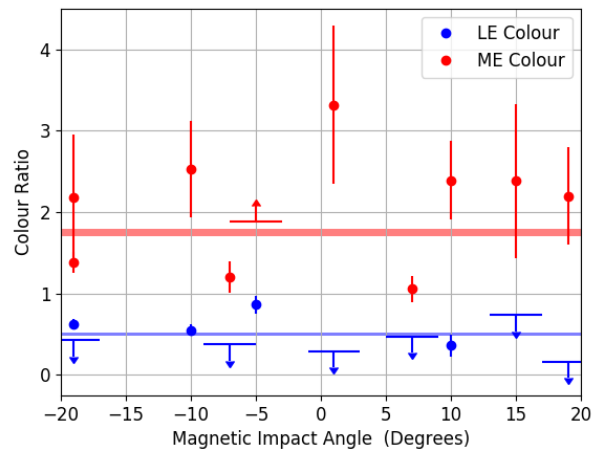
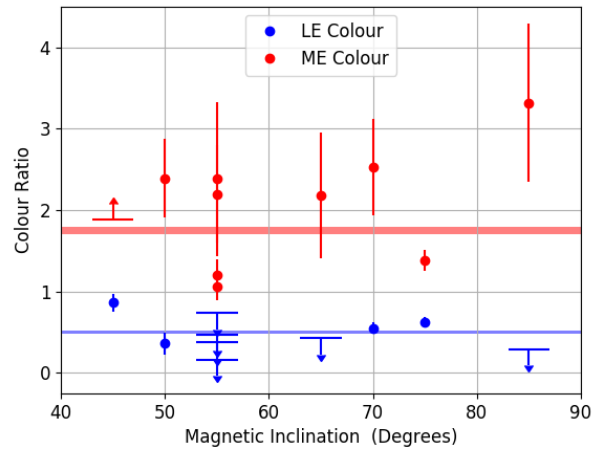
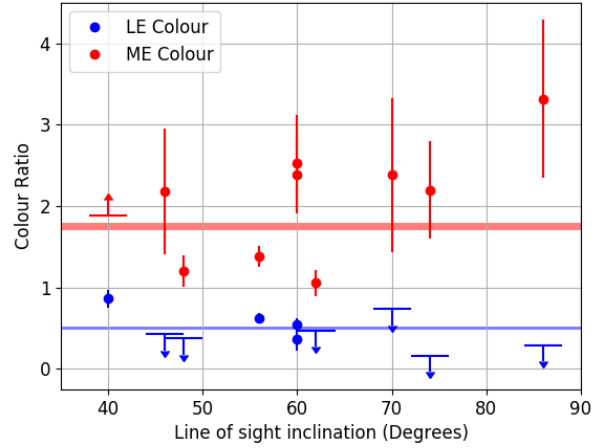


Figure 6. The LE and ME colours for ten MSPs plotted against line of sight inclination (ζ), magnetic inclination (α) from Benli et al. (2021) and magnetic impact angle ($\beta = \text{Line of sight inclination} - \text{magnetic inclination}$). All inclinations are with respect to the pulsar rotational axis. There is no obvious correlation of colour with line of sight or magnetic inclination whilst the magnetic impact angle shows colours with symmetry between 5 and 10° where the colour ratios are close to 1 indicating a harder spectrum. The LP colour values are shown as red and blue bands. Colour ratios are shown either as points with errors, or as upper or lower limits.

pulsar properties affect spectral shape by using energy flux ratios (or colours) for the low-energy (133/237 MeV) and medium energy (4.2/7.5 GeV) bins. We find that pulsar \dot{E} , surface magnetic field and gamma-ray luminosity are uncorrelated with these colours and hence do not systematically affect the spectral shape in the low-energy and medium energy bins. Similarly we find that LE and ME colours, are in the main, uncorrelated with magnetic impact angle, indicating that pulsar spin axis inclination and magnetic inclination have little effect on the LE and ME features of the observed gamma-ray spectrum. There is a hint of symmetry in ME colours for harder emission from magnetic impact angles between 5 and 10°, but more inclination determinations for a larger pulsar sample would be required to confirm this.

In general, our results show little influence on the low and medium energy gamma-ray spectrum arising from pulsar geometry.

Finally, we note that our MSP spectral model (LP) is useful more generally in the problems of the Galactic centre excess and the ensemble emission in globular clusters arising from a population of MSPs.

ACKNOWLEDGEMENTS

We acknowledge the data and tools provided by the *Fermi*-LAT collaboration. AMB and PMC acknowledge the financial support of the UK Science and Technology Facilities Council consolidated grant ST/X001075/1. SJL acknowledges the financial support of Durham University. We thank the anonymous referee for comments which helped improve this paper.

DATA AVAILABILITY STATEMENT

The data underlying this article will be shared on reasonable request to the corresponding author.

APPENDIX A: COMPARISON OF STACKED MODELS OF MSP EMISSION

The 2PC is a published survey of pulsars observed by *Fermi*-LAT. It uses 3 years of *PASS* 7 event data in the energy range between 100 MeV and 100 GeV with the 2FGL source catalog as a source model and lists the spectral models and fluxes of 117 pulsars, evenly divided between MSPs, young radio-quiet and young radio-loud pulsars. The survey uses three search strategies for pulsar detection to overcome the difficulty of only one photon being detected in a few million pulsar rotations. Firstly, the known rotation ephemerides of pulsars, obtained mostly through radio and in some cases X-ray observations, are used to fit a timing model with *TEMPO*/*TEMPO2* software, to tag the gamma-ray event data with a pulsar phase. The gamma-ray data are then phase-folded to identify any emission peaks. Secondly, blind periodicity searches are used on unassociated sources classed as candidate pulsars because they show no variability and have spectra that can be fitted by an exponential cut-off in the GeV band. This method is challenging because the event data are sparse with only a few photons detected per hour and in addition pulsars may have been missed by being in binary systems, which tends to smear the signal through Doppler shifts arising from orbital motion. Finally, the detection of pulsed radio emission in unassociated sources and the construction of timing models can lead to the detection of gamma-ray pulsations through phase folding methods as above. The 2PC lists 40 MSPs, 20 of which have been detected

using this final method. The 2PC increased the then known MSP sample from 8 to 40 MSPs with heliocentric distances up to 2 kpc and a uniform distribution in the sky. The MSPs exhibit between 1–3 gamma-ray peaks and their differential flux spectrum, dN/dE , (photon flux per energy bin) is an exponential cut-off power law as described by Eqn. A1. This equation is functionally equivalent to Eqn. 1 with the exponential factor a replaced by $1/E_{\text{cut}}$ and index γ_1 having negative sign. For consistency with the 2PC and [Xing & Wang \(2016\)](#) we continue to use symbols k , Γ and b which are equivalent to the N_0 , γ_1 and γ_2 in Eqn. 1

$$\frac{dN}{dE} = k \left(\frac{E}{E_0} \right)^{-\Gamma} \exp \left(- \frac{E}{E_{\text{cut}}} \right)^b \quad (\text{A1})$$

$$E^2 \frac{dN}{dE} = k \left(\frac{E}{1 \text{ GeV}} \right)^{\Gamma} \exp \left(- \frac{E}{E_{\text{cut}}} \right)^b \quad (\text{A2})$$

The MSPs listed in the 2PC also provide a pulsar sample to use in determining models of stacked gamma-ray emission. [Xing & Wang \(2016\)](#) re-analyse 39 of the 40 MSPs in the 2PC (excluding one, J1939+2134, which has a detection significance of $\approx 3\sigma$) using 7.5 years of *PASS* 8 event data in the energy range 100 MeV–300 GeV in 15 energy bins, using the 3FGL as a source catalog model.

In the 3FGL, 33 MSPs are described by an exponential cut-off power law model (Eqn. A1), whereas 6 MSPs are best fitted with a simple power law (PL) (Eqn. 3). However, in their analysis they find that an exponential cut-off can be detected in the 6 PL MSPs at $> 3\sigma$ significance. They therefore use an exponential cut-off power law model throughout their analysis. They then stack all flux points from the 39 MSPs with a $TS > 9$ (equivalent to $> 3\sigma$ significance) to obtain a functional form described by an exponential cut-off power law as Eqn. A1 with $\Gamma = 1.54^{+0.10}_{-0.11}$ and $E_{\text{cut}} = 3.70^{+0.95}_{-0.70}$ but with E_0 and b equal to 1 (hereafter the "Xing and Wang" model). Finally, they recommend that this functional form can be used as a model to find candidate MSPs in unidentified *Fermi*-LAT sources at high Galactic latitudes.

Alternatively, [McCann \(2015\)](#) constructs a stacked MSP gamma-ray spectrum using an aperture photometry (AP) method rather than likelihood analysis. The AP approach has the advantage over the likelihood approach in that it is model independent and less computationally intensive. However, it does require timing information for the pulsars analysed. McCann chooses 39 MSPs from the 2PC (excluding a different one, J2215+5135 because its off-phase, where emission is at a minimum, is undefined) and consider 4.2 years of *PASS* 7 event data per MSP in the energy range 100 MeV–1 TeV binned at 4 bins per decade of energy. McCann then uses the *TEMPO* 2 software to barycentre and phase fold the photon events. McCann then obtains the energy excess counts of all events outside the off-phase (i.e the on-phase), distributed by energy, corrects for exposure and produces a spectral energy distribution from the stacked fluxes. Finally McCann fits the differential flux $E^2 \frac{dN}{dE}$ (as opposed $\frac{dN}{dE}$) with an exponential cut-off power law, with a functional form as Eqn. A2. This exponential cut-off power law has $\Gamma = 0.54 \pm 0.05$, $E_{\text{cut}} = 3.60 \pm 0.21$ GeV and $b = 0.7 \pm 0.15$ (hereafter the "McCann" model). McCann also makes a check on the performance of the AP method vs the likelihood method of the 2PC by defining a flux ratio for the MSPs of $\frac{AP \text{ flux}}{2PC \text{ flux}}$ which varies between 0.8 and 0.9 for energies of 250 MeV–8 GeV.

We assess which MSP model(s) (LP, PLSEC, McCann or Xing and Wang) are a preferred description of our stacked MSP spectrum through a likelihood analysis. We allow the normalisation of the models to vary and determine for each normalisation the residual

Parameter	Value	Unit
<i>Index1</i>	-1.28 ± 0.01	-
<i>Normalisation</i>	$(4.75 \pm 0.06) \times 10^{-4}$	$\text{cm}^{-2} \text{s}^{-1} \text{TeV}^{-1}$
<i>Exponential factor</i>	$(3.95 \pm 0.07) \times 10^2$	TeV^{-1}
<i>Index2</i>	1.0	-
<i>Scale</i>	1×10^{-3}	TeV

Table A1. The parameters of the best-fitted PLSEC model (this work) using Eqn. 1, for the stacked differential energy flux of 118 significantly detected MSPs in the energy range 100 MeV–56.2 GeV. This model is inferior to the LP model above.

for each energy bin which is the difference between the stacked MSP flux and the model flux evaluated at the centre of each energy bin in the spectrum. We sum the log of the absolute value of each bin residual to obtain a set of log likelihood values, one for each normalisation. We then determine a minimum log likelihood value of -135.2 , -131.9 , -137.6 and -123.9 for the LP, PLSEC, Xing and Wang, and McCann models, respectively. Using Eqn. 4 and the minimum log likelihood value of each model as L_0 and L_1 , we determine that LP, and Xing and Wang, are significantly preferred over that of McCann at TS 22.6 (4.7σ) and 27.4 (5.2σ) respectively, whilst LP, and Xing and Wang are an equally good fit to the MSP spectrum using a likelihood analysis.

In Fig. 1, we show the likelihood best fit models and the stacked spectrum of 118 MSPs with the LP model fitting the greatest number of flux points.

The preferred MSP model can also be determined using the minimum value of the Akaike Information Criterion (AIC) statistic Akaike (1974), (Eqn. A3). The AIC ranks how well a model fits a data set (compared to other models) and penalises the over-fitting which results from the model having more free parameters. The AIC is a relative measure in that it allows a set of models to be compared with the model exhibiting the lowest AIC score considered superior in that set, but it does not allow a determination of whether any model is best in an absolute sense. The AIC is defined in Eqn. A3 where k is the number of free model parameters and ℓ is the likelihood of the best fit model.

$$AIC = 2k - 2 \ln(\ell) \tag{A3}$$

For the purposes of spectral model comparison, a more convenient definition of AIC is Eqn. A4 where n is the number of flux data points or energy bins and RSS is the residual sum of squares as defined in Eqn. A5 with y_i being the observed flux and $f(x_i)$ the flux predicted by the model for an energy x_i for an energy bin i .

$$AIC = 2k + n \ln \left(\frac{RSS}{n} \right) \tag{A4}$$

$$RSS = \sum_{i=1}^n (y_i - f(x_i))^2 \tag{A5}$$

The AIC statistic for the fit of our models, LP, PLSEC, and the models of Xing and Wang, and McCann, to the stacked MSP spectrum between 100 MeV–56.2 GeV, is -232.7 , -223.9 , -223.1 and -204.4 respectively. Our model, LP, having the minimum AIC statistic, is thus the preferred one. Furthermore the evidential significance Δ_i of any model, i , can be determined as $\Delta_i = (\text{AIC value for model } i - \text{AIC value for our model})$. A Δ_i value ≤ 2 indicates a model has substantial support whereas $\Delta_i \geq 10$ indicates a model

has essentially no support (Burnham & Anderson (2004)). The Δ_i values for Xing and Wang, and McCann are 9.6 and 28.3 respectively and hence these models are disfavoured by the AIC statistic.

The absolute goodness-of-fit of models to the stacked MSPs can also be determined by the χ^2 statistic which we calculate across the energy range of each bin and take the minimum (best) χ^2 value in each bin for the best fit likelihood model. The LP, PLSEC, Xing and Wang and McCann models have a χ^2 statistic of 6.6, 192.0, 1225.5 and 2472.8 respectively between 100 MeV–56.2 GeV (Table A2).

The Xing and Wang model is an acceptable fit from 178 MeV to 56.2 GeV whereas the PLSEC model is an acceptable fit from 562 MeV to 17.8 GeV. The McCann model is not a good fit, with χ^2 values exceeding the critical value in most bins (7 d.o.f. / critical value 24.3 for $\alpha = 0.001$). In contrast, only the LP model provides an acceptable fit across the whole energy range (8 d.o.f. / critical value 26.1 for $\alpha = 0.001$) whilst minimising χ^2 compared to the other models, The LP model is therefore the preferred spectral model overall.

During the final preparation of this paper we became aware of a new MSP spectral model based on 104 MSPs (Wu et al. (2022)) prepared using the same method as Xing & Wang (2016). However, we find that this model is essentially the same as that of Xing & Wang (2016), having log-likelihood = -142.1 and AIC = -221.5 , and similar χ^2 per bin with respect to the critical value as Xing & Wang (2016), so we do not consider it further.

Bin Center MeV	Lower Bin Energy MeV	Upper Bin Energy MeV	LP χ^2	PLSEC χ^2	Xing and Wang χ^2	McCann χ^2
133	100	178	0.0	121.1	1198.1	199.9
237	178	316	0.0	15.6	0.0	101.4
421	316	562	0.0	27.8	0.0	445.3
750	562	1000	0.0	0.0	1.6	631.9
1333	1000	1778	6.6	0.0	20.8	638.7
2371	1778	3162	0.0	0.0	0.0	210.4
4217	3162	5623	0.0	0.0	0.0	0.0
7499	5623	10000	0.0	0.0	0.0	65.5
13335	10000	17783	0.0	0.0	0.0	157.4
23714	17783	31623	0.0	21.5	0.1	22.3
42170	31623	56234	0.0	6.0	4.9	0.0
Total:			6.6	192.0	1225.5	2472.8

Table A2. A breakdown of χ^2 test statistic by energy bin, for stacked models of MSP emission fitted to the 118 MSP stacked flux, ranked in order of total χ^2 . The LP model (this work) is best in minimising χ^2 overall and the only model which provides an acceptable fit across the whole energy range (0.1–56.2 GeV). The McCann model is not a good fit, with χ^2 values exceeding the critical value in most bins (7 d.o.f. / critical value 24.3 for $\alpha = 0.001$). All other models 8 d.o.f. / critical value 26.1 for $\alpha = 0.001$.

APPENDIX B: MSP FLUXES AND DETECTION SIGNIFICANCE

MSP Name	Source ID	TS	Offset (Degrees)	Energy Flux $10^{-11} \text{ erg cm}^{-2} \text{ s}^{-1}$	Photon Flux $10^{-8} \text{ cm}^{-2} \text{ s}^{-1}$
J1921+1929	4FGL J1921.1+1930	27.5	0.058	0.44 ± 0.32	0.52 ± 0.21
J0737-3039A	PS J0738.0-3041	29.3	0.056	0.34 ± 0.09	0.30 ± 0.12
J1137+7528	4FGL J1137.6+7527	29.4	0.043	0.07 ± 0.23	0.03 ± 0.10
J1125-6014	4FGL J1126.4-6011	33.6	0.086	0.28 ± 0.82	0.13 ± 0.25
J1811-2405	4FGL J1811.3-2403	37.3	0.035	0.93 ± 0.18	1.34 ± 0.36
J1833-3840	4FGL J1833.0-3840	54.7	0.012	0.24 ± 0.51	0.19 ± 0.07
J0931-1902	4FGL J0931.2-1906	57.5	0.066	0.16 ± 0.45	0.10 ± 0.29
J0653+4706	4FGL J0652.9+4707	63.4	0.028	0.17 ± 0.04	0.16 ± 0.06
J0248+4230	4FGL J0248.6+4230	75.7	0.021	0.19 ± 0.34	0.17 ± 0.11
J2052+1218	4FGL J2052.7+1218	75.9	0.015	0.49 ± 0.07	0.76 ± 0.16
J1431-4715	4FGL J1431.4-4711	79.0	0.080	0.54 ± 0.07	1.00 ± 0.18
J1855-1436	4FGL J1855.9-1435	83.2	0.017	0.50 ± 1.04	0.37 ± 0.10
J0952-0607	4FGL J0952.1-0607	83.9	0.020	0.22 ± 0.43	0.16 ± 0.07
J1730-2304	4FGL J1730.8-2303	87.8	0.106	0.76 ± 0.61	1.05 ± 0.16
J1908+2105	4FGL J1908.9+2103	90.2	0.020	0.54 ± 0.22	0.55 ± 0.07
J2051-0827	4FGL J2051.0-0826	91.4	0.028	0.25 ± 0.56	0.12 ± 0.28
J1555-2908	4FGL J1555.7-2908	92.8	0.006	0.57 ± 0.07	0.96 ± 0.15
J1640+2224	4FGL J1640.1+2222	103.5	0.047	0.27 ± 0.36	0.29 ± 0.08
J1544+4937	4FGL J1544.0+4939	105.9	0.022	0.23 ± 0.06	0.22 ± 0.06
J0621+2514	4FGL J0621.2+2512	115.3	0.026	0.48 ± 0.51	0.30 ± 0.04
J2006+0148	4FGL J2006.4+0147	117.5	0.022	0.39 ± 0.14	0.21 ± 0.06
J2039-3616	4FGL J2039.4-3616	120.1	0.029	0.37 ± 0.50	0.47 ± 0.15
J1641+8049	4FGL J1641.2+8049	132.5	0.006	0.22 ± 0.08	0.23 ± 0.05
J2047+1053	4FGL J2047.3+1051	133.0	0.058	0.43 ± 0.44	0.32 ± 0.02
J1732-5049	4FGL J1732.7-5050	144.7	0.021	0.56 ± 0.68	0.62 ± 0.13
J1741+1351	4FGL J1741.4+1354	147.0	0.051	0.43 ± 0.06	0.31 ± 0.08
J1125-5825	4FGL J1125.6-5825	149.7	0.012	0.59 ± 0.71	0.37 ± 0.09
J1805+0615	4FGL J1805.6+0615	165.3	0.007	0.53 ± 0.79	0.36 ± 0.11
J1939+2134	4FGL J1939.6+2135	178.0	0.016	1.97 ± 0.33	3.04 ± 0.43
J1552+5437	4FGL J1553.1+5438	181.4	0.042	0.28 ± 0.26	0.23 ± 0.05
J1824+1014	4FGL J1824.1+1013	185.1	0.021	0.59 ± 0.71	0.44 ± 0.04
J0740+6620	4FGL J0741.0+6618	192.5	0.038	0.30 ± 1.09	0.28 ± 0.10
J1036-8317	4FGL J1036.5-8318	195.7	0.013	0.44 ± 0.05	0.30 ± 0.06
J1024-0719	4FGL J1024.5-0719	200.6	0.034	0.43 ± 0.54	0.44 ± 0.12
J2115+5448	4FGL J2115.1+5449	205.9	0.014	0.80 ± 0.28	0.48 ± 0.03
J1335-5656	4FGL J1335.0-5656	211.8	0.017	0.87 ± 0.43	0.71 ± 0.31

continued ...

... continued

MSP Name	Source ID	TS	Offset (Degrees)	Energy Flux $10^{-11} \text{ erg cm}^{-2} \text{ s}^{-1}$	Photon Flux $10^{-8} \text{ cm}^{-2} \text{ s}^{-1}$
J1012-4235	4FGL J1012.1-4235	218.5	0.011	0.52 ± 0.05	0.50 ± 0.09
J1921+0137	4FGL J1921.4+0136	226.5	0.027	1.04 ± 0.22	1.07 ± 0.18
J1207-5050	4FGL J1207.4-5050	232.7	0.012	0.53 ± 0.06	0.44 ± 0.11
J0955-6150	4FGL J0955.4-6151	238.0	0.024	0.69 ± 0.55	0.77 ± 0.06
J0251+2606	4FGL J0251.0+2605	239.0	0.007	0.50 ± 0.43	0.47 ± 0.04
J1446-4701	4FGL J1446.6-4701	240.2	0.008	0.63 ± 0.73	0.57 ± 0.12
J1827-0849	4FGL J1827.6-0849	243.9	0.008	2.31 ± 1.85	2.50 ± 0.58
J1048+2339	4FGL J1048.6+2340	250.0	0.021	0.56 ± 0.05	0.93 ± 0.14
J2042+0246	4FGL J2042.2+0245	263.6	0.074	0.62 ± 0.37	0.80 ± 0.05
J1543-5149	4FGL J1543.6-5148	270.8	0.016	1.66 ± 1.09	2.43 ± 0.31
J2017-1614	4FGL J2017.7-1612	271.1	0.036	0.65 ± 0.49	0.69 ± 0.18
J0318+0253	4FGL J0318.2+0254	279.1	0.028	0.59 ± 0.60	0.58 ± 0.15
J1843-1113	4FGL J1843.7-1114	282.1	0.021	1.71 ± 1.16	3.05 ± 0.47
J1400-1431	4FGL J1400.6-1432	294.6	0.019	0.66 ± 0.07	0.77 ± 0.15
J1649-3012	4FGL J1649.8-3010	302.6	0.032	0.97 ± 0.73	1.10 ± 0.23
J1622-0315	4FGL J1623.0-0315	321.7	0.004	0.91 ± 0.66	1.10 ± 0.25
J0605+3757	4FGL J0605.1+3757	326.4	0.009	0.67 ± 0.07	0.42 ± 0.04
J0312-0921	4FGL J0312.1-0921	327.3	0.016	0.51 ± 0.05	0.31 ± 0.05
J2129-0429	4FGL J2129.8-0428	328.5	0.026	0.58 ± 0.69	0.51 ± 0.14
J1713+0747	4FGL J1713.8+0747	331.7	0.010	0.77 ± 0.07	0.65 ± 0.11
J1513-2550	4FGL J1513.4-2549	351.4	0.024	0.75 ± 0.69	0.76 ± 0.15
J1221-0633	4FGL J1221.4-0634	356.4	0.031	0.68 ± 0.70	0.76 ± 0.16
J1903-7051	4FGL J1903.4-7053	360.0	0.033	0.58 ± 0.06	0.48 ± 0.09
J1628-3205	4FGL J1628.1-3204	374.1	0.026	1.14 ± 0.57	1.56 ± 0.29
J1142+0119	4FGL J1142.8+0120	385.2	0.011	0.66 ± 0.07	0.57 ± 0.11
J1901-0125	4FGL J1901.4-0126	394.1	0.028	1.91 ± 1.31	2.52 ± 0.28
J2310-0555	4FGL J2310.0-0555	402.4	0.013	0.76 ± 0.07	0.96 ± 0.16
J1747-4036	4FGL J1747.7-4037	410.9	0.004	1.28 ± 0.79	1.67 ± 0.21
J0610-2100	4FGL J0610.2-2100	411.4	0.010	0.68 ± 0.40	0.72 ± 0.28
J1600-3053	4FGL J1600.9-3054	422.0	0.012	0.85 ± 0.69	0.47 ± 0.03
J0023+0923	4FGL J0023.4+0920	426.5	0.053	0.82 ± 0.06	0.94 ± 0.13
J1745+1017	4FGL J1745.5+1017	432.9	0.011	0.88 ± 0.78	0.72 ± 0.14
J1630+3734	4FGL J1630.6+3734	441.3	0.010	0.55 ± 0.52	0.42 ± 0.10
J2034+3632	4FGL J2035.0+3632	483.2	0.006	1.26 ± 0.77	0.40 ± 0.12
J1301+0833	4FGL J1301.6+0834	496.0	0.005	0.79 ± 0.27	0.83 ± 0.12
J2256-1024	4FGL J2256.8-1024	520.7	0.014	0.81 ± 0.72	0.92 ± 0.07
J1823-3021A	4FGL J1823.5-3020	534.1	0.027	1.41 ± 1.09	1.39 ± 0.18
J1858-2216	4FGL J1858.3-2216	586.8	0.005	1.13 ± 0.58	0.89 ± 0.05
J1959+2048	4FGL J1959.5+2048	615.5	0.009	1.58 ± 0.54	1.97 ± 0.16
J0418+6635	4FGL J0418.9+6636	621.9	0.014	1.10 ± 0.09	0.89 ± 0.14
J0533+6759	4FGL J0533.8+6800	635.5	0.012	0.88 ± 0.06	0.85 ± 0.10
J2234+0944	4FGL J2234.7+0943	643.9	0.012	1.07 ± 0.08	0.82 ± 0.11
J1824-2452A	4FGL J1824.6-2452	718.7	0.028	2.10 ± 1.07	2.85 ± 0.27
J0751+1807	4FGL J0751.2+1808	819.4	0.016	1.04 ± 0.08	0.63 ± 0.10
J1946-5403	4FGL J1946.5-5402	826.3	0.011	1.04 ± 0.06	1.21 ± 0.13
J1302-3258	4FGL J1302.4-3258	848.1	0.015	1.12 ± 0.77	0.73 ± 0.20
J1658-5324	4FGL J1658.6-5323	985.9	0.007	2.04 ± 0.97	2.84 ± 0.50
J0102+4839	4FGL J0102.8+4839	1036.5	0.003	1.43 ± 0.84	1.49 ± 0.15
J1816+4510	4FGL J1816.5+4510	1043.4	0.007	1.00 ± 0.06	0.99 ± 0.09
J1124-3653	4FGL J1124.0-3653	1060.3	0.015	1.37 ± 0.85	1.19 ± 0.05
J1312+0051	4FGL J1312.7+0050	1204.1	0.008	1.38 ± 0.68	1.38 ± 0.10
J2039-5617	4FGL J2039.5-5617	1205.7	0.007	1.50 ± 0.74	1.90 ± 0.09
J2215+5135	4FGL J2215.6+5135	1211.9	0.008	1.83 ± 0.09	2.00 ± 0.15
J1035-6720	4FGL J1035.4-6720	1485.3	0.003	1.94 ± 0.58	1.81 ± 0.09
J0307+7443	4FGL J0307.8+7443	1560.8	0.004	1.59 ± 0.80	1.32 ± 0.25
J0340+4130	4FGL J0340.3+4130	1577.4	0.001	1.90 ± 1.31	1.06 ± 0.18
J1810+1744	4FGL J1810.5+1744	1610.4	0.012	2.29 ± 0.34	3.68 ± 0.28
J1227-4853	4FGL J1228.0-4853	1625.6	0.020	2.29 ± 0.24	3.61 ± 0.34

continued ...

... continued

MSP Name	Source ID	TS	Offset (Degrees)	Energy Flux $10^{-11} \text{ erg cm}^{-2} \text{ s}^{-1}$	Photon Flux $10^{-8} \text{ cm}^{-2} \text{ s}^{-1}$
J1744-7619	4FGL J1744.0-7618	1784.1	0.005	1.99 ± 0.08	1.74 ± 0.12
J0101-6422	4FGL J0101.1-6422	1822.7	0.012	1.33 ± 0.74	1.53 ± 0.13
J1625-0021	4FGL J1625.1-0020	1878.4	0.011	2.14 ± 0.11	1.64 ± 0.15
J0034-0534	4FGL J0034.3-0534	1961.0	0.006	2.02 ± 1.16	2.67 ± 0.39
J1614-2230	4FGL J1614.5-2230	2177.6	0.010	2.59 ± 1.19	1.70 ± 0.08
J1902-5105	4FGL J1902.0-5105	2290.1	0.010	2.45 ± 0.64	3.86 ± 0.17
J1744-1134	4FGL J1744.4-1135	2328.5	0.009	3.88 ± 1.01	4.35 ± 0.20
J1653-0158	4FGL J1653.6-0158	2422.3	0.011	3.35 ± 0.10	4.84 ± 0.22
J2043+1711	4FGL J2043.3+1711	2478.1	0.004	2.66 ± 0.66	2.66 ± 0.21
J0613-0200	4FGL J0613.7-0201	2678.6	0.014	3.82 ± 0.12	4.85 ± 0.22
J0437-4715	4FGL J0437.2-4715	3019.1	0.006	1.73 ± 0.06	2.74 ± 0.13
J2339-0533	4FGL J2339.6-0533	3058.5	0.001	2.73 ± 0.12	2.55 ± 0.15
J2241-5236	4FGL J2241.7-5236	3063.8	0.005	2.59 ± 0.91	2.05 ± 0.27
J1514-4946	4FGL J1514.3-4946	3105.5	0.003	4.07 ± 1.14	3.06 ± 0.13
J2017+0603	4FGL J2017.4+0602	3174.7	0.012	3.56 ± 0.15	1.96 ± 0.13
J2214+3000	4FGL J2214.6+3000	4809.6	0.009	3.20 ± 0.09	2.63 ± 0.11
J2302+4442	4FGL J2302.7+4443	4991.6	0.010	3.66 ± 0.10	2.79 ± 0.11
J2124-3358	4FGL J2124.7-3358	5935.9	0.010	3.94 ± 1.50	2.93 ± 0.43
J1536-4948	4FGL J1536.4-4948	6600.5	0.004	7.96 ± 0.59	7.24 ± 0.24
J0218+4232	4FGL J0218.1+4232	6771.2	0.007	4.97 ± 0.10	8.32 ± 0.22
J1311-3430	4FGL J1311.7-3430	9011.3	0.007	6.23 ± 0.38	8.49 ± 0.26
J0030+0451	4FGL J0030.4+0451	10547.1	0.001	5.89 ± 1.53	6.21 ± 0.33
J1231-1411	4FGL J1231.1-1412	18868.5	0.002	10.20 ± 0.18	7.61 ± 0.16
J0614-3329	4FGL J0614.1-3329	26170.5	0.003	11.34 ± 0.20	7.87 ± 0.14

Table B1: Analysis results for all significantly detected MSPs, in the energy range 100 MeV–100 GeV, with 4FGL source id, detection significance (TS), offset from catalogue co-ordinates and fluxes.

APPENDIX C: DETECTED MSP SPECTRAL PARAMETERS AND EXEMPLAR SPECTRA

MSP Name	Prefactor 10^{-13}	Index1	Scale	Expfactor 10^{-3}
J1921+1929	7.48 ± 8.30	-1.16 ± 0.31	3061	11.46 ± 0.00
J1137+7528	3.46 ± 14.25	0.00 ± 0.01	3077	13.03 ± 4.65
J1125-6014	22.07 ± 69.17	-0.01 ± 1.08	2576	15.66 ± 0.39
J1833-3840	17.35 ± 42.02	-0.57 ± 1.73	1538	14.85 ± 0.00
J0931-1902	25.90 ± 74.11	0.00 ± 0.01	1926	19.91 ± 0.05
J0653+4706	66.48 ± 51.65	0.00 ± 0.03	1321	26.28 ± 5.31
J0248+4230	25.53 ± 61.13	-0.35 ± 1.24	1961	19.33 ± 0.04
J1855-1436	5.21 ± 11.29	-1.24 ± 1.26	2051	5.68 ± 0.00
J0952-0607	29.92 ± 66.18	-0.20 ± 1.78	1583	18.71 ± 0.05
J1730-2304	156.25 ± 207.42	-0.69 ± 0.87	1251	22.97 ± 0.00
J1908+2105	6.36 ± 3.59	-1.34 ± 0.23	2223	7.13 ± 0.15
J2051-0827	21.52 ± 48.11	0.00 ± 0.01	2105	16.05 ± 0.16
J1640+2224	9.66 ± 18.85	-1.05 ± 1.23	1763	11.67 ± 0.07
J1544+4937	4.43 ± 0.99	-1.47 ± 0.20	1193	5.00 ± 0.01
J0621+2514	33.52 ± 52.22	-0.27 ± 1.13	2653	15.36 ± 0.02
J2006+0148	4.76 ± 1.75	-0.84 ± 0.26	2658	7.44 ± 0.00
J2039-3616	17.97 ± 29.87	-1.20 ± 1.03	1300	11.88 ± 0.77
J1641+8049	8.35 ± 4.13	-1.05 ± 0.33	1663	11.65 ± 0.02
J2047+1053	5.50 ± 5.97	-1.17 ± 0.72	1964	6.41 ± 0.01
J1732-5049	14.56 ± 24.84	-1.23 ± 1.01	1684	9.65 ± 0.01
J1741+1351	12.33 ± 3.46	-0.97 ± 0.23	1372	8.62 ± 1.79
J1125-5825	11.91 ± 20.67	-0.71 ± 0.98	3232	10.33 ± 0.09
J1805+0615	27.56 ± 43.89	-0.54 ± 1.13	1750	13.16 ± 0.02

continued ...

... continued

MSP Name	Prefactor 10^{-13}	Index1	Scale	Expfactor 10^{-3}
J1939+2134	53.65 ± 14.00	-1.38 ± 0.12	1892	12.35 ± 0.01
J1552+5437	7.19 ± 5.90	-1.14 ± 0.64	1318	7.66 ± 0.04
J1824+1014	13.25 ± 15.49	-1.02 ± 0.94	1619	8.16 ± 0.01
J0740+6620	10.19 ± 39.13	-1.11 ± 2.75	1340	9.45 ± 0.05
J1036-8317	19.50 ± 2.14	-0.63 ± 0.14	1787	12.37 ± 0.00
J1024-0719	22.60 ± 32.71	-0.99 ± 0.99	1305	12.12 ± 0.04
J2115+5448	11.10 ± 5.30	-0.80 ± 0.23	3387	8.84 ± 0.10
J1012-4235	8.50 ± 0.95	-1.27 ± 0.12	1849	7.45 ± 0.01
J1921+0137	15.57 ± 4.21	-1.34 ± 0.17	1871	7.16 ± 0.01
J1207-5050	38.90 ± 31.00	-0.55 ± 0.45	1950	15.72 ± 4.66
J0955-6150	25.58 ± 23.25	-1.23 ± 0.63	1256	9.56 ± 0.01
J0251+2606	67.61 ± 70.78	-0.46 ± 0.87	1361	18.64 ± 0.00
J1446-4701	25.87 ± 31.74	-0.95 ± 0.91	1450	11.01 ± 0.26
J1827-0849	15.66 ± 19.05	-1.55 ± 0.69	2349	5.00 ± 0.02
J1048+2339	15.05 ± 2.95	-1.85 ± 0.14	1013	5.77 ± 1.50
J2042+0246	235.13 ± 219.24	-0.39 ± 0.81	1080	27.00 ± 0.01
J1543-5149	40.13 ± 45.76	-1.48 ± 0.65	1582	9.57 ± 0.00
J2017-1614	12.20 ± 12.01	-1.35 ± 0.78	1608	7.28 ± 0.01
J0318+0253	42.08 ± 56.41	-0.74 ± 0.82	1645	15.32 ± 0.20
J1843-1113	90.51 ± 97.67	-1.59 ± 0.68	1017	11.42 ± 0.02
J1649-3012	48.30 ± 48.51	-1.03 ± 0.58	1512	12.89 ± 0.05
J1622-0315	17.45 ± 17.08	-1.50 ± 0.76	1433	6.69 ± 0.02
J0605+3757	97.79 ± 9.51	0.00 ± 0.00	1904	19.08 ± 0.01
J2129-0429	34.71 ± 38.50	-0.83 ± 0.86	1186	12.28 ± 0.06
J1713+0747	32.93 ± 8.76	-0.84 ± 0.19	1603	11.78 ± 1.67
J1513-2550	38.30 ± 41.98	-0.97 ± 0.74	1375	12.25 ± 0.02
J1221-0633	32.53 ± 35.06	-1.19 ± 0.79	1123	10.44 ± 0.30
J1903-7051	16.52 ± 6.18	-0.90 ± 0.24	2071	10.69 ± 1.99
J1628-3205	77.18 ± 57.57	-1.09 ± 0.40	1400	15.21 ± 0.04
J1142+0119	12.33 ± 2.42	-1.27 ± 0.17	1436	6.32 ± 1.22
J1901-0125	43.79 ± 43.07	-1.48 ± 0.61	1453	8.08 ± 0.02
J2310-0555	20.35 ± 7.16	-1.50 ± 0.22	1207	7.23 ± 2.55
J1747-4036	71.71 ± 68.54	-1.10 ± 0.57	1471	14.04 ± 0.00
J0610-2100	49.28 ± 46.63	-0.91 ± 1.04	1182	13.79 ± 1.49
J1600-3053	25.06 ± 22.43	-0.54 ± 0.62	2399	10.96 ± 0.01
J0023+0923	62.43 ± 12.22	-1.05 ± 0.15	973	12.70 ± 1.66
J1745+1017	56.02 ± 55.83	-0.65 ± 0.71	1532	13.97 ± 0.01
J1630+3734	68.71 ± 70.94	-0.30 ± 0.82	1465	18.06 ± 0.02
J1301+0833	56.21 ± 19.61	-0.96 ± 0.25	1077	12.94 ± 0.02
J2256-1024	44.90 ± 39.07	-1.20 ± 0.76	981	10.32 ± 0.00
J1823-3021A	20.72 ± 20.29	-1.30 ± 0.53	1940	7.23 ± 0.06
J1858-2216	120.63 ± 81.44	-0.36 ± 0.50	1794	17.55 ± 0.01
J1959+2048	103.95 ± 48.94	-1.05 ± 0.28	1308	14.14 ± 0.00
J0533+6759	16.26 ± 3.02	-1.32 ± 0.12	1536	6.78 ± 1.12
J2234+0944	31.34 ± 6.17	-0.92 ± 0.14	1647	9.70 ± 1.19
J1824-2452A	75.64 ± 56.68	-1.34 ± 0.44	1399	10.75 ± 0.01
J0751+1807	57.62 ± 18.00	-0.37 ± 0.21	2271	14.00 ± 1.61
J1946-5403	68.30 ± 20.78	-0.95 ± 0.17	1472	14.72 ± 2.07
J1302-3258	53.93 ± 41.62	-0.55 ± 0.88	1667	12.51 ± 0.64
J1658-5324	275.92 ± 182.74	-0.91 ± 0.38	1136	19.04 ± 0.02
J0102+4839	30.06 ± 19.17	-1.39 ± 0.51	1362	6.65 ± 0.00
J1816+4510	42.73 ± 5.21	-1.09 ± 0.10	1211	10.15 ± 0.89
J1124-3653	42.93 ± 26.38	-1.06 ± 0.50	1391	9.15 ± 0.06
J1312+0051	109.13 ± 68.36	-0.77 ± 0.54	1353	15.08 ± 0.01
J2039-5617	43.88 ± 24.27	-1.53 ± 0.43	1098	6.85 ± 0.01
J2215+5135	29.76 ± 2.36	-1.45 ± 0.06	1565	6.31 ± 0.46
J1035-6720	135.86 ± 53.04	-0.71 ± 0.25	1615	15.01 ± 0.00
J0307+7443	182.07 ± 106.38	-0.41 ± 0.35	1549	17.79 ± 0.03

continued ...

... continued

MSP Name	Prefactor 10^{-13}	Index1	Scale	Expfactor 10^{-3}
J0340+4130	55.67 ± 32.52	-0.66 ± 0.43	1637	9.82 ± 0.00
J1810+1744	108.13 ± 20.20	-1.61 ± 0.12	944	9.08 ± 0.01
J1227-4853	25.71 ± 3.91	-1.82 ± 0.09	1597	5.29 ± 0.00
J1744-7619	181.73 ± 29.36	-0.60 ± 0.11	1273	15.64 ± 1.20
J0101-6422	110.28 ± 58.12	-1.06 ± 0.46	898	12.69 ± 0.02
J1625-0021	111.50 ± 29.82	-0.70 ± 0.17	1481	12.56 ± 1.78
J0034-0534	127.77 ± 63.82	-1.48 ± 0.38	732	8.06 ± 0.01
J1614-2230	183.68 ± 92.25	-0.37 ± 0.42	1771	14.89 ± 0.01
J1902-5105	94.38 ± 37.34	-1.58 ± 0.29	1083	9.12 ± 0.00
J1744-1134	954.11 ± 300.05	-0.45 ± 0.27	1033	22.73 ± 0.00
J1653-0158	215.58 ± 6.77	-1.47 ± 0.04	820	9.61 ± 0.00
J2043+1711	86.28 ± 21.19	-1.23 ± 0.16	1212	8.35 ± 0.01
J0613-0200	176.02 ± 5.59	-1.38 ± 0.03	1001	9.13 ± 0.00
J0437-4715	574.20 ± 57.88	-0.88 ± 0.08	624	23.04 ± 1.21
J2339-0533	76.33 ± 7.56	-1.33 ± 0.07	1063	6.36 ± 0.73
J2241-5236	144.93 ± 60.61	-0.62 ± 0.22	1880	13.93 ± 0.02
J1514-4946	87.27 ± 23.63	-1.05 ± 0.17	1627	7.92 ± 0.00
J2017+0603	80.12 ± 9.03	-0.75 ± 0.08	1741	8.67 ± 0.65
J2214+3000	280.87 ± 7.96	-0.60 ± 0.04	1092	14.71 ± 0.00
J2302+4442	164.61 ± 4.38	-0.81 ± 0.03	1292	11.00 ± 0.00
J2124-3358	396.58 ± 131.19	-0.42 ± 0.24	1125	15.96 ± 0.00
J1536-4948	123.55 ± 8.81	-1.39 ± 0.05	1445	5.38 ± 0.00
J0218+4232	226.13 ± 4.97	-1.80 ± 0.02	802	6.54 ± 0.00
J1311-3430	263.06 ± 15.13	-1.64 ± 0.04	812	6.04 ± 0.00
J0030+0451	577.90 ± 141.06	-0.87 ± 0.21	930	14.43 ± 0.00
J1231-1411	692.13 ± 11.07	-0.65 ± 0.02	1057	12.83 ± 0.00
J0614-3329	337.66 ± 4.79	-1.03 ± 0.02	1070	7.40 ± 0.00

Table C1: The spectral parameters for 108 MSPs, in the energy range 100 MeV–100 GeV, described by a PLSuperExp2 spectral model, in order of increasing detection significance. The *index2* parameter (not shown) has value 0.67 throughout.

MSP Name	Norm 10^{-13}	Alpha	Beta	Eb
J1335-5656	6.95 ± 2.49	2.06 ± 0.13	0.29 ± 0.09	1547
J1400-1431	14.54 ± 1.53	2.13 ± 0.12	0.34 ± 0.10	987
J0312-0921	12.35 ± 1.42	1.80 ± 0.19	0.94 ± 0.24	1179
J2034+3632	6.09 ± 3.89	2.11 ± 0.62	0.97 ± 0.02	2678
J0418+6635	9.15 ± 0.66	2.04 ± 0.08	0.29 ± 0.06	1525

Table C2: The spectral parameters for MSPs, in the energy range 100 MeV–100 GeV, with a LP spectral model, in order of increasing detection significance.

MSP Name	Prefactor 10^{-13}	Index1	Scale
J0737-3039A	3.02 ± 0.82	-1.98 ± 0.15	1000
J1811-2405	0.78 ± 0.18	-2.22 ± 0.12	3126
J2052+1218	3.68 ± 0.55	-2.27 ± 0.11	1165
J1431-4715	8.07 ± 1.09	-2.38 ± 0.10	868
J1555-2908	10.26 ± 1.27	-2.31 ± 0.09	801

Table C3: The spectral parameters for MSPs, in the energy range 100 MeV–100 GeV, with a PL spectral model, in order of increasing detection significance.

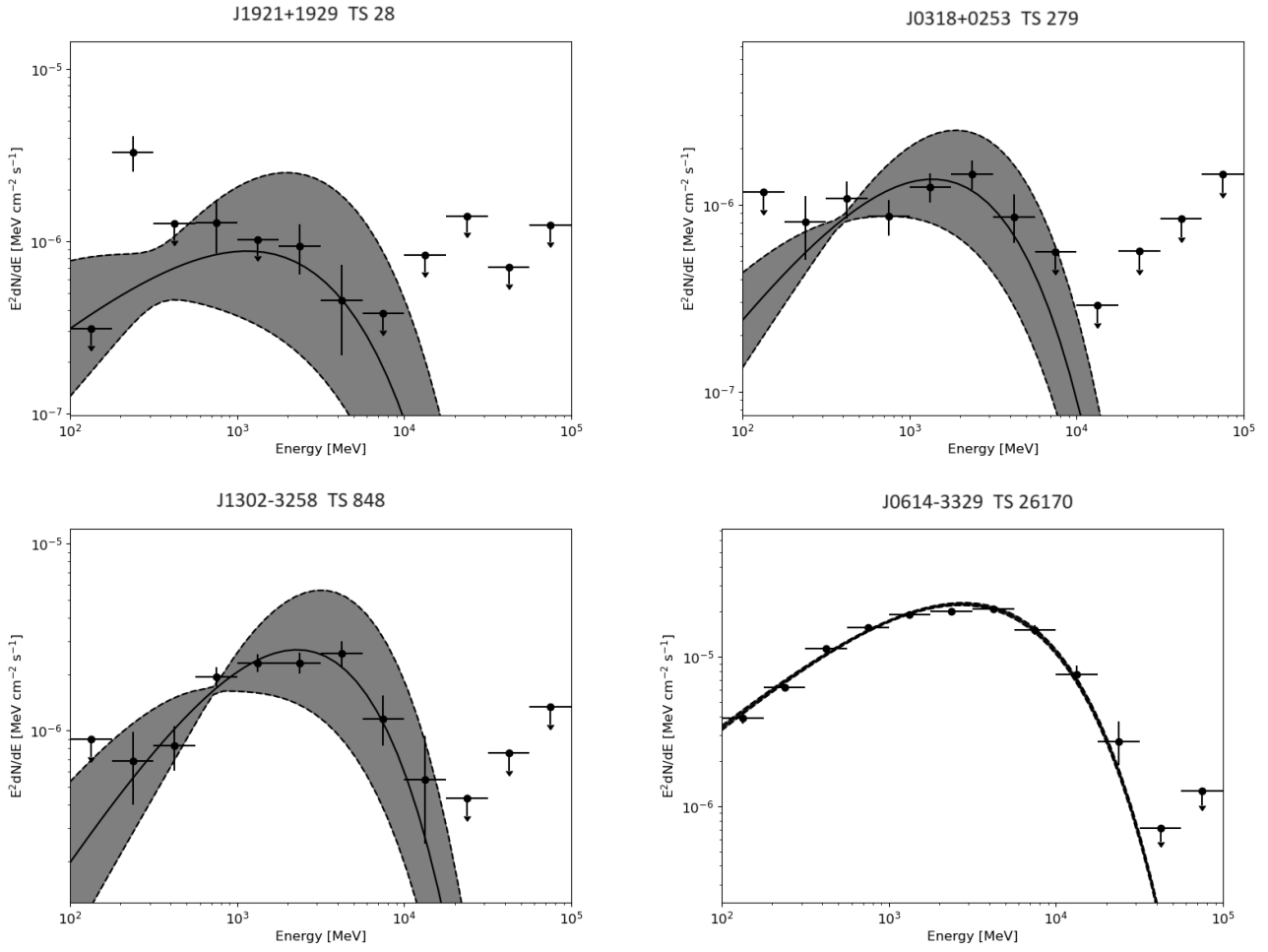


Figure C1. Individual MSP spectra fitted with a PLSuperExp2 spectral model. The examples here range from the lowest to highest detection significance (TS).

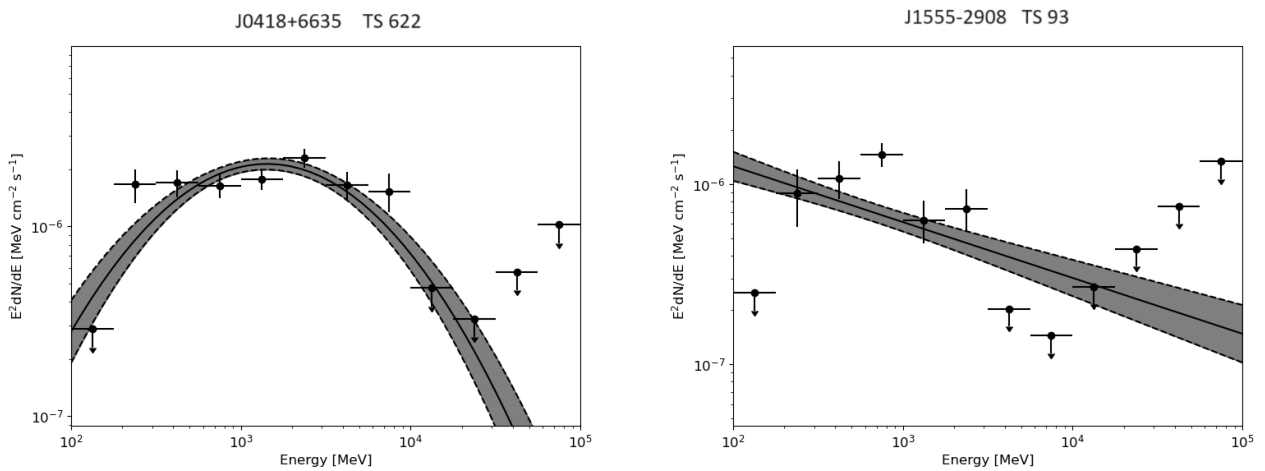


Figure C2. Individual MSP spectra fitted with a log parabola (left) and power law model (right). The examples here are those with the highest detection significance.

APPENDIX D: LIST OF SELECTED MSPS

MSP Name	RA (Deg.)	DEC (Deg.)	Period (ms)	\dot{E} $10^{34} \text{ erg s}^{-1}$
J0931-1902	142.83	-19.05	4.64	0.14
J1730-2304	262.59	-23.08	8.12	0.15
J1455-3330	223.95	-33.51	7.99	0.19
J1207-5050	181.84	-50.84	4.84	0.21
J2317+1439	349.29	14.66	3.45	0.23
J1640+2224	250.07	22.4	3.16	0.35
J1713+0747	258.46	7.79	4.57	0.35
J0030+0451	7.61	4.86	4.87	0.35
J1327-0755	201.99	-7.93	2.68	0.37
J1744-7619	266	-76.32	4.69	0.37
J2302+4442	345.7	44.71	5.19	0.37
J1732-5049	263.2	-50.82	5.31	0.37
J1946+3417	296.6	34.29	3.17	0.39
J1142+0119	175.71	1.33	5.08	0.45
J1744-1134	266.12	-11.58	4.07	0.52
J1745+1017	266.39	10.3	2.65	0.53
J1024-0719	156.16	-7.32	5.16	0.53
J1946-5403	296.64	-54.06	2.71	0.54
J2051-0827	312.78	-8.46	4.51	0.55
J0636+5129	99.02	51.48	2.87	0.57
J0533+6759	83.48	67.99	4.39	0.57
J0737-3039A	114.46	-30.66	22.7	0.59
J2042+0246	310.5	2.8	4.53	0.6
J2124-3358	321.18	-33.98	4.93	0.69
J0751+1807	117.79	18.13	3.48	0.73
J0340+4130	55.1	41.51	3.3	0.75
J1552+5437	238.22	54.62	2.43	0.77
J2017-1614	304.44	-16.24	2.31	0.78
J1137+7528	174.26	75.47	2.51	0.79
J1622-0315	245.75	-3.26	3.85	0.79
J1125-6014	171.48	-60.24	2.63	0.81
J1600-3053	240.22	-30.9	3.6	0.81
J0610-2100	92.56	-21.01	3.86	0.84
J1012-4235	153.05	-42.6	3.1	0.87
J1855-1436	283.98	-14.6	3.59	0.93
J1312+0051	198.19	0.85	4.23	0.93
J0605+3757	91.27	37.96	2.73	0.95
J1400-1431	210.15	-14.53	3.08	0.97
J1858-2216	284.57	-22.28	2.38	1.1
J0101-6422	15.3	-64.38	2.57	1.1
J2310-0555	347.53	-5.93	2.61	1.1
J1630+3734	247.65	37.58	3.32	1.1
J2047+1053	311.79	10.89	4.29	1.1
J1653-0158	253.41	-1.98	1.97	1.2
J1544+4937	236.02	49.63	2.16	1.2
J1048+2339	162.18	23.66	4.67	1.2
J0437-4715	69.32	-47.25	5.76	1.2
J2017+0603	304.34	6.05	2.9	1.3
J1614-2230	243.65	-22.51	3.15	1.3
J2043+1711	310.84	17.19	2.38	1.5
J0023+0923	5.82	9.39	3.05	1.5
J0613-0200	93.43	-2.01	3.06	1.5
J1514-4946	228.58	-49.77	3.59	1.6
J2234+0944	338.7	9.74	3.63	1.6
J1124-3653	171	-36.89	2.41	1.7
J1832-0836	278.11	-8.62	2.72	1.7

continued ...

... continued

MSP Name	RA (Deg.)	DEC (Deg.)	Period (ms)	\dot{E} $10^{34} \text{ erg s}^{-1}$
J0102+4839	15.71	48.66	2.96	1.7
J2214+3000	333.66	30.01	3.12	1.8
J1231-1411	187.8	-14.2	3.68	1.8
J0740+6620	115.19	66.34	2.89	2
J2339-0533	354.91	-5.55	2.88	2.2
J1909-3744	287.45	-37.74	2.95	2.2
J0614-3329	93.54	-33.5	3.15	2.2
J0307+7443	46.98	74.72	3.16	2.2
J1741+1351	265.38	13.86	3.75	2.2
J2241-5236	340.43	-52.61	2.19	2.5
J1811-2405	272.83	-24.09	2.66	2.8
J0034-0534	8.59	-5.58	1.88	2.9
J1536-4948	234.1	-49.82	3.08	2.9
J2039-5617	309.9	-56.29	2.65	3
J1036-8317	159.17	-83.3	3.41	3
J1658-5324	254.66	-53.4	2.44	3.2
J1446-4701	221.65	-47.02	2.19	3.8
J1827-0849	276.9	-8.83	2.24	3.8
J0248+4230	42.13	42.51	2.6	3.8
J1810+1744	272.66	17.74	1.66	4
J0621+2514	95.3	25.23	2.72	4.8
J1921+0137	290.38	1.62	2.5	4.9
J1311-3430	197.94	-34.51	2.56	4.9
J2215+5135	333.89	51.59	2.61	5.2
J1816+4510	274.15	45.18	3.19	5.2
J1843-1113	280.92	-11.23	1.85	6
J1901-0125	285.39	-1.42	2.79	6.5
J0952-0607	148.03	-6.12	1.41	6.7
J1902-5105	285.51	-51.1	1.74	6.8
J1431-4715	217.94	-47.26	2.01	6.8
J0955-6150	148.83	-61.84	2	7
J1543-5149	235.93	-51.83	2.06	7.3
J1035-6720	158.86	-67.34	2.87	7.7
J1921+1929	290.35	19.49	2.65	8.1
J1125-5825	171.43	-58.42	3.1	8.1
J1227-4853	186.99	-48.9	1.69	9
J1513-2550	228.35	-25.84	2.12	9
J1903-7051	285.91	-70.86	3.6	9.9
J1747-4036	266.95	-40.62	1.65	12
J1959+2048	299.9	20.8	1.61	16
J2115+5448	318.8	54.81	2.6	17
J0218+4232	34.53	42.54	2.32	24
J1555-2908	238.92	-29.14	1.79	31
J1823-3021A	275.92	-30.36	5.44	83
J1939+2134	294.91	21.58	1.56	110
J1824-2452A	276.13	-24.87	3.05	220
J1301+0833	195.41	8.57	1.84	–
J1833-3840	278.27	-38.68	1.87	–
J1221-0633	185.35	-6.56	1.93	–
J2052+1218	313.2	12.33	1.99	–
J1641+8049	250.34	80.83	2.02	–
J1805+0615	271.43	6.26	2.13	–
J2006+0148	301.62	1.82	2.16	–
J2256-1024	344.23	-10.41	2.29	–
J0154+1833	28.65	18.56	2.36	–
J2205+6012	331.39	60.22	2.42	–
J0251+2606	42.76	26.1	2.54	–
J1908+2105	287.24	21.08	2.56	–

continued ...

... continued

MSP Name	RA (Deg.)	DEC (Deg.)	Period (ms)	\dot{E} $10^{34} \text{ erg s}^{-1}$
J1625-0021	246.29	-0.36	2.83	–
J0418+6635	64.7	66.59	2.91	–
J1628-3205	247.03	-32.1	3.21	–
J1335-5656	203.77	-56.93	3.24	–
J2039-3616	309.82	-36.27	3.28	–
J1649-3012	252.44	-30.21	3.42	–
J2034+3632	308.75	36.54	3.65	–
J0312-0921	48.03	-9.37	3.7	–
J1302-3258	195.61	-32.98	3.77	–
J1824+1014	276.06	10.25	4.07	–
J0653+4706	103.27	47.11	4.76	–
J0318+0253	49.56	2.88	5.19	–
J2129-0429	322.44	-4.49	7.61	–

Table D1: Analysis selection of 127 MSPs from the "Public List of LAT-Detected Gamma-Ray Pulsars" ordered by \dot{E} . RAJ and DECJ are right ascension and declination in degrees. 25 MSPs have no \dot{E} given in the online catalogue as indicated by a "–".

REFERENCES

- Abazajian K. N., 2011, *Journal of Cosmology and Astroparticle Physics*
- Abdo A. A., et al., 2009a, *Science*, 325, 845
- Abdo A. A., et al., 2009b, *Science*, 325, 848
- Abdo A. A., et al., 2013, *Astrophysical Journal Supplement Series*, 208, 59
- Ajello M., et al., 2017, *Astrophysical Journal Supplement Series*, 232
- Akaike H., 1974, *IEEE Transactions on Automatic Control*, 19, 716
- Bartels R., Edwards T., 2019, *Physical Review D*, 100
- Benli O., Petri J., Mitra D., 2021, *Astronomy & Astrophysics*, 647
- Brown A. M., Lacroix T., Lloyd S., Boehm C., Chadwick P., 2018, *Physical Review D*, 98
- Brown A. M., Lacroix T., Lloyd S., Boehm C., Chadwick P., 2019, *Physical Review D*, 100
- Burnham K. P., Anderson D. R., 2004, *Sociological Methods & Research*, 33, 261
- Cerutti B., Philippov A. A., Spitkovsky A., 2016, *Monthly Notices of the Royal Astronomical Society*, 457, 2401
- Deutsch A. J., 1955, *Annales d'Astrophysique*, 18, 1
- FSSC 2010, https://fermi.gsfc.nasa.gov/ssc/data/analysis/scitools/source_models.html
- Giraud Q., Petri J., 2021, *Astronomy & Astrophysics*, 654
- Guillemot L., Tauris T. M., 2014, *Monthly Notices of the Royal Astronomical Society*, 439, 2033
- Guillemot L., et al., 2016, *Astronomy & Astrophysics*, 587
- Johnson T. J., et al., 2014, *Astrophysical Journal Supplement Series*, 213
- McCann A., 2015, *Astrophysical Journal*, 804, 10
- Muslimov A. G., Harding A. K., 2004, *The Astrophysical Journal*, 617, 471
- Petri J., 2019, *Monthly Notices of the Royal Astronomical Society*, 484, 5669
- Ploeg H., Gordon C., Crocker R., Macias O., 2020, *Journal of Cosmology and Astroparticle Physics*, 2020, 035
- Smith D. A., Guillemot L., Kerr M., Ng C., Barr E., 2017, Gamma-ray pulsars with Fermi ([arXiv:1706.03592](https://arxiv.org/abs/1706.03592)), <https://arxiv.org/abs/1706.03592>
- Smith D. A., et al., 2019, *Astrophysical Journal*, 871
- Smith D. A., et al., 2023, *Astrophysical Journal*, 958
- Torres D. F., Vigano D., Zelati F. C., Li J., 2019, *Monthly Notices of the Royal Astronomical Society*, 489, 5494
- Vigano D., Torres D. F., Hirotani K., Pessah M. E., 2015a, *Monthly Notices of the Royal Astronomical Society*, 447, 2631
- Vigano D., Torres D. F., Hirotani K., Pessah M. E., 2015b, *Monthly Notices of the Royal Astronomical Society*, 447, 2649
- Wood M., Caputo R., Charles E., Di Mauro M., Magill J., Jeremy Perkins for the Fermi-LAT Collaboration 2017, preprint, ([arXiv:1707.09551](https://arxiv.org/abs/1707.09551))
- Wu W., Wang Z., Xing Y., Zhang P., 2022, *The Astrophysical Journal*, 927, 117
- Xing Y., Wang Z. X., 2016, *Astrophysical Journal*, 831, 8
- Zhang L., Cheng K. S., 2003, *Astronomy & Astrophysics*, 398, 639

This paper has been typeset from a $\text{\TeX}/\text{\LaTeX}$ file prepared by the author.